



AFRL-RW-EG-TR-2016-088

Near-Resonant Thermomechanics of Energetic and Mock Energetic Composite Materials

**Jeffrey F. Rhoads, Steven F. Son,
Patricia Davies, Marcial Gonzalez,
Marisol Koslowski, Allison Range,
Jelena Paripovic, Ankit Agarwal,
Bogdan Tanasoiu, Johanna Palsdottir**

**School of Mechanical Engineering
Purdue University
585 Purdue Mall
West Lafayette, IN 47907**

Contract No. FA8651-16-0287

November 2016

Final Report

**Distribution A: Approved for public release; distribution unlimited.
Approval Confirmation 96TW-2016-0227 dated 08 December 2016**

AIR FORCE RESEARCH LABORATORY, MUNITIONS DIRECTORATE

Air Force Materiel Command • United States Air Force • Eglin Air Force Base

NOTICE AND SIGNATURE PAGE

Using Government drawings, specifications, or other data included in this document for any purpose other than Government procurement does not in any way obligate the U.S. Government. The fact that the Government formulated or supplied the drawings, specifications, or other data does not license the holder or any other person or corporation; or convey any rights or permission to manufacture, use, or sell any patented invention that may relate to them.

Qualified requestors may obtain copies of this report from the Defense Technical Information Center (DTIC) (<http://www.dtic.mil>).

AFRL-RW-EG-TR-2016-088 HAS BEEN REVIEWED AND IS APPROVED FOR PUBLICATION IN ACCORDANCE WITH ASSIGNED DISTRIBUTION STATEMENT.

FOR THE DIRECTOR:

//SIGNED//

//SIGNED//

//SIGNED//

JOHN D. CORLEY, PhD
Ordnance Sciences Core
Technical Competency Lead
Ordnance Division

C. MICHAEL LINDSAY, PhD
Technical Advisor
Energetic Materials Branch

BRETT KIZER
Work Unit Manager
Energetic Materials Branch

This report is published in the interest of scientific and technical information exchange, and its publication does not constitute the Government's approval or disapproval of its ideas or findings.

This page intentionally left blank

REPORT DOCUMENTATION PAGE

Form Approved

OMB No. 0704-

Public reporting burden for this collection of information is estimated to average 1 hour per response, including the time for reviewing instructions, searching existing data sources, gathering and maintaining the data needed, and completing and reviewing this collection of information. Send comments regarding this burden estimate or any other aspect of this collection of information, including suggestions for reducing this burden to Department of Defense, Washington Headquarters Services, Directorate for Information Operations and Reports (0704-0188), 1215 Jefferson Davis Highway, Suite 1204, Arlington, VA 22202-4302. Respondents should be aware that notwithstanding any other provision of law, no person shall be subject to any penalty for failing to comply with a collection of information if it does not display a currently valid OMB control number. PLEASE DO NOT RETURN YOUR FORM TO THE ABOVE ADDRESS.

1. REPORT DATE (DD-MM-YYYY) 30-11-2016			2. REPORT TYPE Final		3. DATES COVERED (From - To) 26 October 2015 – 25 October 2016	
4. TITLE AND SUBTITLE Near-Resonant Thermomechanics of Energetic and Mock Energetic Composite Materials			5a. CONTRACT NUMBER FA8651-16-D-0287			
			5b. GRANT NUMBER			
			5c. PROGRAM ELEMENT NUMBER 62602F			
6. AUTHOR(S) Jeffrey F. Rhoads, Steven F. Son, Patricia Davies, Marcial Gonzalez, Marisol Koslowski, Allison Range, Jelena Paripovic, Ankit Agarwal, Bogdan Tanasoiu, Johanna Palsdottir			5d. PROJECT NUMBER 25029969			
			5e. TASK NUMBER			
			5f. WORK UNIT NUMBER W0XJ			
7. PERFORMING ORGANIZATION NAME(S) AND ADDRESS(ES) School of Mechanical Engineering Purdue University 585 Purdue Mall West Lafayette, IN 47907			8. PERFORMING ORGANIZATION REPORT NUMBER			
9. SPONSORING / MONITORING AGENCY NAME(S) AND ADDRESS(ES) Air Force Research Laboratory, Munitions Directorate Ordnance Division Energetic Materials Branch (AFRL/RWME) Eglin AFB FL 32542-5910 Technical Advisor: C. Michael Lindsay, PhD			10. SPONSOR/MONITOR'S ACRONYM(S) AFRL-RW-EG			
			11. SPONSOR/MONITOR'S REPORT NUMBER(S) AFRL-RW-EG-TR-2016-088			
12. DISTRIBUTION / AVAILABILITY STATEMENT Distribution A: Approved for public release; distribution unlimited. Approval Confirmation 96TW-2016-0227 dated 08 December 2016						
13. SUPPLEMENTARY NOTES		SUBJECT TO EXPORT CONTROL LAWS DISTRIBUTION STATEMENT INDICATING AUTHORIZED ACCESS IS ON THE COVER PAGE AND BLOCK 12 OF THIS FORM. DATA RIGHTS RESTRICTIONS AND AVAILABILITY OF THIS REPORT ARE SHOWN ON THE NOTICE AND SIGNATURE PAGE.				
14. ABSTRACT The effort described herein seeks to explore the near-resonant thermomechanics of energetic and mock energetic particulate composite materials. The effort specifically focuses on: (i) characterizing the macroscale, elastic and plastic responses of these materials under various mechanical excitations at a range of ambient temperatures; and (ii) developing preliminary computational modeling tools, which can be used to predict material response during energetic material formulation and munition design.						
15. SUBJECT TERMS Energetic Materials; Explosives; Mechanical Vibration; Thermomechanics; Damping; Plasticity						
16. SECURITY CLASSIFICATION OF:			17. LIMITATION OF ABSTRACT	18. NUMBER OF PAGES	19a. NAME OF RESPONSIBLE PERSON Steven J. Pemberton	
a. REPORT UNCLASSIFIED	b. ABSTRACT UNCLASSIFIED	c. THIS PAGE UNCLASSIFIED	SAR	64	19b. TELEPHONE NUMBER (include area code) 850-882-1195	

This page intentionally left blank

TABLE OF CONTENTS

Section	Page
1.0 SUMMARY	1
2.0 INTRODUCTION	1
3.0 METHODS, ASSUMPTIONS, AND PROCEDURES.....	2
3.1 Sample Preparation	2
3.2 Microscale Thermomechanical Testing	5
3.3 Dissipative Modeling and Material Property Parameter Estimation	6
3.4 Endochronic Plasticity Modeling.....	7
3.5 Crystal-Binder Interface Modeling.....	8
4.0 RESULTS AND DISCUSSION	9
4.1 Macroscale Thermomechanical Testing Results	9
4.2 Dissipative Modeling and Material Property Parameter Estimation	15
4.3 Endochronic Plasticity Modeling.....	18
4.4 Crystal-Binder Interface Results.....	20
5.0 CONCLUSIONS.....	21
6.0 REFERENCES	21
APPENDIX.....	24

LIST OF FIGURES

Figure		Page
1	Mold assembly for the 2.54 cm diameter, 2.54 cm height cylindrical samples.....	3
2	Mold assembly for the 7.62 cm diameter, 7.62 cm height cylindrical samples.....	3
3	Mold assembly for the 17.78 cm x 25.4 cm x 1.27 cm rectangular plate samples	4
4	Labeled schematic of the experimental setup used under ambient environmental conditions	6
5	Experimental H1 mechanical frequency response estimator for a 50% solids loading plate obtained at three levels of excitation. The blue, green, and red curves depict responses at 1, 1.86, and 2.44 g RMS, respectively. Solid lines represent data from the geometric center, and dashed lines represent data from the offset point	9
6	Experimental H1 mechanical frequency response estimator for a 65% solids loading plate obtained at three levels of excitation. The blue, green, and red curves depict responses at 1, 1.86, and 2.44 g RMS, respectively. Solid lines represent data from the geometric center, and dashed lines represent data from the offset point	10
7	Experimental H1 mechanical frequency response estimator for a 75% solids loading plate obtained at three levels of excitation. The blue, green, and red curves depict responses at 1, 1.86, and 2.44 g RMS, respectively. Solid lines represent data from the geometric center, and dashed lines represent data from the offset point	10
8	Experimentally-obtained mean plate surface temperature shown as a function of time	11
9	Experimentally-obtained maximum plate surface temperature shown as a function of time	11
10	Simulated mean plate surface temperature shown as a function of time	13
11	Simulated maximum plate surface temperature shown as a function of time	13
12	Experimental H1 mechanical frequency response estimator obtained for an 85% solids loading - 0% additive content plate at three levels of excitation. The blue, green, and red curves depict responses at 1, 1.86, and 2.44 g RMS, respectively. Solid lines represent data from the geometric center, and dashed lines represent data from the offset point.....	14
13	Experimental H1 mechanical frequency response estimator obtained for an 85% solids loading - 30% additive content plate at three levels of excitation. The blue, green, and red curves depict responses at 1, 1.86, and 2.44 g RMS, respectively. Solid lines represent data from the geometric center, and dashed lines represent data from the offset point.....	14
14	Experimentally-obtained mean plate surface temperature shown as a function of time	15

LIST OF FIGURES (cont)

Figure	Page
15 Experimentally-obtained maximum plate surface temperature shown as a function of time.....	15
16 (a) A spectrogram of the response of the mass-material system undergoing swept sine excitation. (b) The response at the excitation frequency. The sample is a 76.2 mm (3 in) sample of HTPB with 0% solids loading excited at 2 g	16
17 (a) The experimentally-obtained relative acceleration signal envelope (blue) and the predicted envelopes from the estimated models: Model 1 (green), 4 (red), 6 (black) and 7 (purple). (b) The information in sub-figure (a) expanded close to the resonance of the system. The sample here is HTPB with 50% solids loading excited at 5 g; estimation data: 3 swept sine tests at 5 g, 7.5 g and 10 g base excitation levels	18
18 (a) Uniaxial constant strain amplitude cyclic hardening response of OFHC copper [endochronic model (solid line) vs experimental data (symbols)]. (b) Prediction of the shear stress versus shear strain of biaxial non-proportional loading of the OFHC copper [endochronic model (solid line) vs experimental data (dashed line)].....	19
19 Force displacement curves used for the calibration of the elastic constant of Sylgard. The experiments were performed by the Son and Chen groups at Purdue University	20
20 A contour plot of the damage field for an applied displacement of 800 μm displacement on top of the domain	20
21 (a) Experiment and (b) simulation of debonding for a 624 μm displacement applied vertically.....	21

LIST OF TABLES

Table	Page
1 PBXN-109 Formulation.....	2
2 Sample Preparation Record as of September 27, 2016.....	4
3 A comparison of the experimentally-obtained plate surface temperature increases under insulated and ambient thermal boundary conditions in response to a 2 g excitation near the first resonant frequency for all of the plates	12
4 Model numbers and corresponding model structure.....	17
5 The elastic constants for Sylgard and glass used in the simulations.....	20

1. SUMMARY

The effort described herein seeks to explore the near-resonant thermomechanics of energetic and mock energetic particulate composite materials. The effort specifically focuses on: (i) characterizing the macroscale, elastic and plastic responses of these materials under various mechanical excitations at a range of ambient temperatures; and (ii) developing preliminary computational modeling tools, which can be used to predict material response during energetic material formulation and munition design. Key topics described herein include: sample preparation; macroscale thermomechanical modeling and experimentation; dissipative modeling and system identification; endochronic plasticity modeling; and crystal-binder interface modeling.

2. INTRODUCTION

The effort described herein seeks to explore the near-resonant thermomechanics of energetic and mock energetic particulate composite materials, building upon both the prior work of the PIs (see, for example, [1-6]) and prior, related work in the field pertaining to the periodic excitation of energetic materials (see, for example, [7-8]) and hot-spot formation (see, for example, [9]). The effort specifically focuses on: (i) characterizing the macroscale, elastic and plastic responses of these materials under various mechanical excitations at a range of ambient temperatures; and (ii) developing preliminary computational modeling tools, which can be used to predict material response during energetic material formulation and munition design. More specifically, Task Order 0001 spans three inter-related research tasks:

- Task 1 – Macroscale Structural and Mechanical Modeling: This task emphasizes further development of macroscale, distributed-parameter and lumped-mass, combined structural and thermal models of mock energetic and energetic materials subjected to mechanical vibration. The models are designed to be amenable to a variety of particle/binder material systems, a range of input excitations, and various ambient temperatures.
- Task 2 – Modeling of Damping and Dissipation: This task emphasizes the development of refined, macroscale dissipation/damping models for mock energetic and energetic materials subjected to mechanical vibration.
- Task 3 – Computational Mechanics Tool Development: This task emphasizes the development of constitutive models for mock energetic and energetic materials that account for nonlinear stress-strain dependencies due to damage, rate-dependent and rate-independent dissipative properties, as well as temperature-dependent properties, and their distillation into computational tools suitable for use in energetic material formulation or munition design.

This final report details the various advancements made by the principal investigators and their research assistants over the noted period of performance. The reader should note that all of the research activities described herein are continuing, in a *big-picture sense*, under Task Order 0002, and thus the methodologies, results, and perspectives detailed herein represent only a *snapshot of ongoing research*.

The subsequent sections are organized in a traditional sense with methodologies, key results, and discussion provided in turn. Discussions of sample preparation; macroscale thermomechanical modeling and experimentation; dissipative modeling and system identification; endochronic plasticity modeling; and crystal-binder interface modeling are provided in Sections 3 and 4. Please note that detailed derivations related to the dissipative modeling and system identification, as well as the endochronic plasticity modeling, are presented in the Appendix to enhance the flow of the report.

3. METHODS, ASSUMPTIONS, AND PROCEDURES

3.1 Sample Preparation

Mock energetic materials in a variety of geometries have been fabricated with the goal of studying the effect of formulation on bulk heating due to mechanical vibration. The formulation variations are based upon the PBXN-109 formulation given by Hamshere et al. [10], with sugar replacing the RDX unless otherwise noted. A summary of this base formulation is given in Table 1.

Table 1. PBXN-109 Formulation

Constituent	Weight Percent
RDX	64.00%
Aluminum	20.00%
R45-HT (Hydroxyl-terminated Polybutadiene Resin)	7.346%
Diethyl Adipate (DOA)	7.346%
Antioxidant 2246	0.100%
Dantocol DHE	0.260%
Triphenylbismuth	0.020%
Isophorone Diisocyanate (IPDI)	0.950%

The base formulation given above was varied based on two parameters, as defined below. Each parameter is being studied at three levels, yielding a sample matrix of seven possible mock energetic formulations.

1. Solids Loading (a metric to indicate the amount of the mixture comprised of "solid" powder): Levels – 0%, 50%, and 85%.
2. Additive Content (a metric to indicate the amount of powder in the mixture is comprised of aluminum): Levels – 0%, 15%, and 30%.

The formulations are cast into three mold geometries. Both small and large cylinders are prepared for uniaxial compression tests in order to determine material properties and model behavior. Plate geometries are prepared for harmonic base excitation tests to investigate thermal and mechanical response at the bulk scale. The mold assemblies used are shown in Figures 1-3.

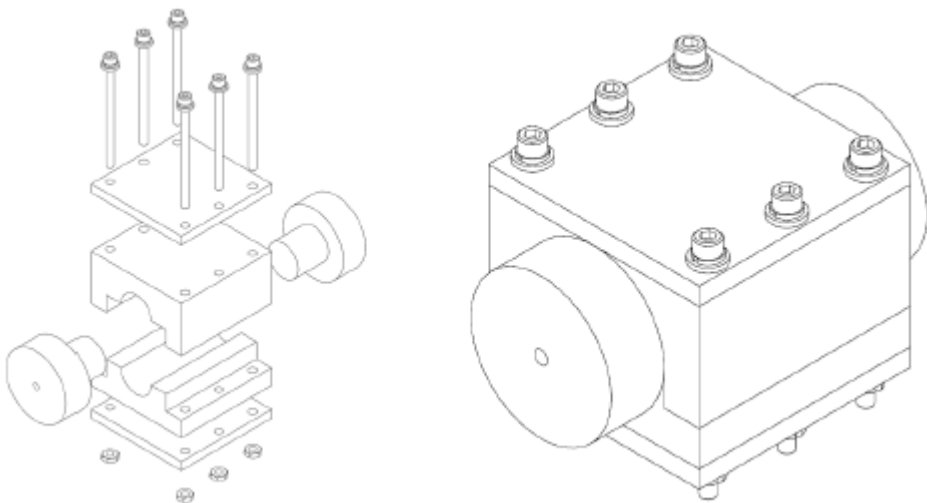


Figure 1. Mold assembly for the 2.54 cm diameter, 2.54 cm height cylindrical samples

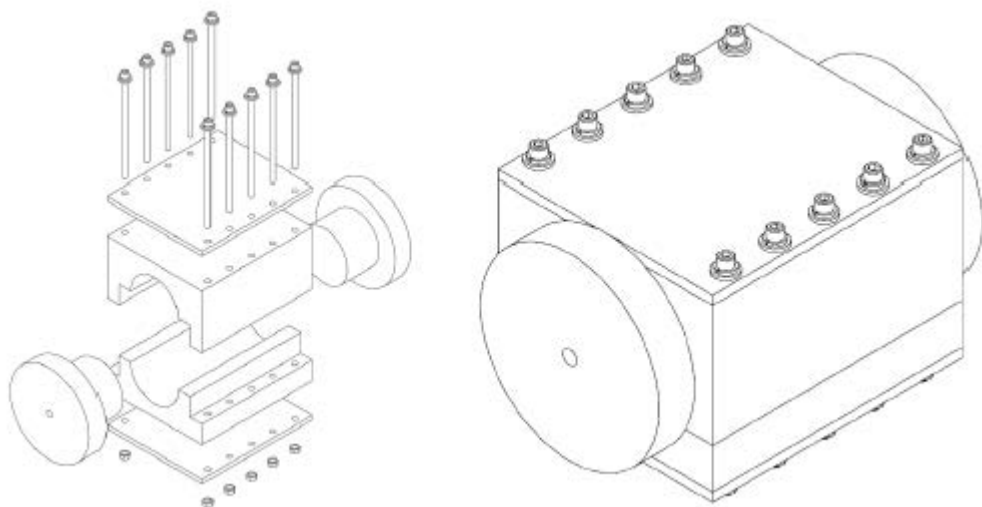


Figure 2. Mold assembly for the 7.62 cm diameter, 7.62 cm height cylindrical samples

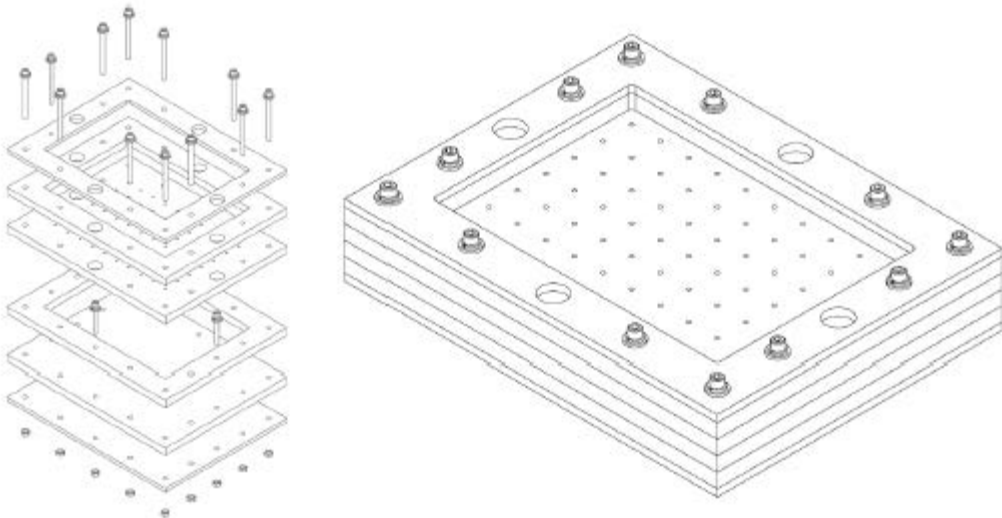


Figure 3. Mold assembly for the 17.78 cm x 25.4 cm x 1.27 cm rectangular plate samples

Two samples of each geometry are cast, yielding a sample set of 6 samples per formulation. The samples successfully fabricated at this time are summarized in Table 2. The 50% solids loading samples are slated to be completed in the coming months. An issue of solids settling out of the binder during curing must be addressed at the lower solids loading before fabrication. Current research seeks to "pre-cure" the HTPB binder to increase its effective viscosity, allowing it to hold the solids in suspension long enough for solidification to occur.

Table 2. Sample Preparation Record as of September 27, 2016

Formulation	Samples Cured
0% Solids Loading	(2) 2.54 cm diameter/height cylinders
0% Additive Content	(2) 7.62 cm diameter/height cylinders
	(2) 17.78 cm x 25.4 cm x 1.27 cm plates
50% Solids Loading	(1) 2.54 cm diameter/height cylinder
0% Additive Content	(1) 7.62 cm diameter/height cylinder
	(1) 17.78 cm x 25.4 cm x 1.27 cm plate
85% Solids Loading	(2) 2.54 cm diameter/height cylinders
0% Additive Content	(2) 7.62 cm diameter/height cylinders
	(2) 17.78 cm x 25.4 cm x 1.27 cm plates
85% Solids Loading	(2) 2.54 cm diameter/height cylinders
15% Additive Content	(2) 7.62 cm diameter/height cylinders
	(2) 17.78 cm x 25.4 cm x 1.27 cm plates
85% Solids Loading	(2) 2.54 cm diameter/height cylinders
30% Additive Content	(2) 7.62 cm diameter/height cylinders
	(2) 17.78 cm x 25.4 cm x 1.27 cm plates

In regards to the fabrication process, binder constituents are mixed manually until coarsely combined. A Resodyn acoustic mixer is then employed to develop a nominally homogeneous mixture (samples are mixed for 5 min at a constant intensity of 80%). The solids are then added into the mixture, and the Resodyn process is repeated once again. The formulation is then transferred into the molds described above and cured in an oven at 60 °C for 7 days.

3.2 Macroscale Thermomechanical Testing

Numerous efforts have been made to increase the understanding of particulate composite mock energetic plates under mechanical vibration. As part of this effort, experiments were conducted on previously-fabricated plate samples in order to investigate the effect of thermal boundary conditions on the thermal response of representative samples. The investigation into the effect of formulation variation on the thermal and mechanical response has also begun, with the results gathered to date being described in the following sections.

As alluded to above, harmonic base excitation experiments were performed in order to investigate the effect of thermal boundary conditions on the vibration-based heating of particulate composite plates. The plate samples tested consisted of HTPB with varying ratios of embedded ammonium chloride crystal, which were chosen as a rough mechanical mock for ammonium perchlorate (AP). Details on these samples can be found in References [3] and [4]. These samples were tested under both ambient and insulated environmental conditions.

Ambient experiments were conducted using three major pieces of equipment. The plate samples were mounted in a pre-existing fixture to approximate a clamped-free-clamped-free (CFCF) boundary configuration and placed upon a TIRA 59335/LS AIT-440 electrodynamic shaker. A Polytec PSV-400 scanning laser Doppler vibrometer was then employed to record frequency responses and operational deflection shapes. Simultaneously, a FLIR A325 infrared camera was used to capture the temperature distribution of the top surface of the plate using infrared thermography. The experimental setup is depicted in Figure 4. The results obtained from this and related testing can be found in Section 4.1.



Figure 4. Labeled schematic of the experimental setup used under ambient environmental conditions

3.3 Dissipative Modeling and Material Property Parameter Estimation

The PBXN-109 samples described above are being tested under this portion of the described research effort with an aim towards dissipative modeling and material property parameter estimation. Both random and harmonic base excitation tests have been conducted on the 25.4 and 76.2 mm (1 and 3 in.) tall/diameter samples with excitations over the frequency range from 10 to 1000 Hz. Base excitation is provided by the aforementioned TIRA electrodynamic shaker and the samples are loaded with a mass and constrained to move uni-axially. The geometry, composition, and cure-date of the samples, as well as a testing progress summary are included in Table A1 in the Appendix.

It should be noted that a day of harmonic base excitation testing consists of 3 sweeps through resonance 30 min apart at 1 g, 2 g, 3 g, or 5 g. Currently we are conducting two excitation level tests on the same day and the tests are ordered as *low, low, high, high, low, high* (where *low* denotes the lower excitation level and *high* the higher). This will allow us to examine same day repeatability and observe if the order of the base excitation level affects the mass-material system response. A day of random base excitation consists of 3 tests with excitation over the range from 10 Hz to 1000 Hz. Testing levels are specified by the power spectral density level in the frequency range of the excitation. Levels being used are $0.015 \text{ g}^2/\text{Hz}$, $0.025 \text{ g}^2/\text{Hz}$, or $0.050 \text{ g}^2/\text{Hz}$. The duration of each test is 100 s. Note that in the course of testing, some excitation levels had to be adjusted to avoid samples fracturing. The mass loading of the samples was also adjusted so that the static strain levels were similar for both sizes of samples.

Note that details of the models and the iterative system identification process that is used to extract the material parameters from the experiments described in this section are provided in the Appendix.

3.4 Endochronic Plasticity Modeling

Energetic composite materials may exhibit significant nonlinear stress-strain response under load, without a distinctive yield surface. As a result, linear material assumptions and classical plasticity theories may prove to be insufficient in predicting their mechanical response, necessitating the use of a plasticity theory that does not include the notion of a yield surface. The endochronic theory of plasticity developed by Valanis [11] is a hereditary plasticity theory that falls into this category. The theory is hereditary in the sense that the state of stress in the neighborhood of a plastic material point depends on the strain or deformation history of that point. The strain history is represented by a variable called intrinsic time, and the stress evolution is given by the convolution integral between the strain tensor and the memory kernel, which is a scalar function of intrinsic time. For a plastically incompressible, rate-independent, and initially isotropic material, the endochronic constitutive equation is given by

$$\mathbf{s} = 2 \int_0^z \rho(z - z') \frac{d\boldsymbol{\epsilon}^p}{dz'} dz' \quad (1)$$

where z is called the intrinsic time scale, $\rho(z)$ is the kernel function and \mathbf{s} is the deviatoric stress given by

$$\mathbf{s} = \boldsymbol{\sigma} - \frac{1}{3} \text{tr}(\boldsymbol{\sigma}) \mathbf{I} \quad (2)$$

and $\boldsymbol{\epsilon}^p$ is the plastic strain. The total strain $\boldsymbol{\epsilon}$ is given by

$$\boldsymbol{\epsilon} = \boldsymbol{\epsilon}^e + \boldsymbol{\epsilon}^p \quad (3)$$

where $\boldsymbol{\epsilon}^e$ the elastic strain, related to the stress $\boldsymbol{\sigma}$ by the elastic stress-strain relationship

$$\boldsymbol{\sigma} = \lambda \text{tr}(\boldsymbol{\epsilon}^e) + 2\mu \boldsymbol{\epsilon}^e \quad (4)$$

where λ and μ are the Lame's constants.

The intrinsic time scale z is related to another variable ζ and a function $f(\zeta)$ by the relation

$$dz = \frac{d\zeta}{f(\zeta)} \quad (5)$$

where ζ is called the intrinsic time measure and is a representative of the plastic strain history in the form

$$d\zeta = \sqrt{d\boldsymbol{\epsilon}^p : d\boldsymbol{\epsilon}^p} \quad (6)$$

and $f(\zeta)$ is called the hardening function and represents the hardening or softening behavior of the material. Thus, the intrinsic time scale z incorporates both strain history and material hardening or softening. Researchers have successfully used this theory to model the inelastic behavior of many materials like metals [12,13], concrete [14], soils [15], metal matrix composites [16], filled rubber [17], Asphalt [18], etc., which confirms the validity of the model and its applicability to our problem. Therefore, endochronic theory has been chosen as the basis of our predictive computational tool for energetic composite materials.

In order to formulate a computationally-efficient and robust tool, the endochronic theory has been implemented in the form of a numerical scheme reported by Hsu et al. [19], which consists of numerical integration of the endochronic constitutive equations in 3D. The scheme has been modified to include rate-dependent (viscoplastic) effects. In addition, an efficient staggered algorithm has been developed for simultaneous calibration of the hardening and kernel functions. The complete numerical scheme along with calibration procedure has been described in the Appendix.

3.5 Crystal-Binder Interface Modeling

There are well-established classical experimental and analytical studies, which explore the bonding between polymers and rigid particles. However, most numerical studies of fracture in composite materials use particle/matrix interface cohesive laws and parameters extracted from the cohesive energy at the macroscale level. While such an approach enables good results when the mechanical response is compared to macroscale experiments, in high-energy composites where the localization of energy dissipation by delamination and friction may lead to the initiation of hot spots, the local particle/matrix cohesive law is of extreme importance. In this work, a systematic numerical study is performed to establish a cohesive law of the composite components and interfaces and to obtain the fracture energy.

Cohesive zone models have been very successful in simulating fracture in many types of composite materials [20], especially when cracks nucleate and propagate along the interfaces [21,22]. In contrast, phase field descriptions of damage have an advantage in problems where the crack path is unknown *a priori* [23,24]. PBXs are a special class of composites in which matrix, particles, and interfaces are prone to fracture, and therefore a phase field approach is more effective. The purpose of this work was to determine the cohesive law for particle, matrix and interfaces using a phase field damage mechanics (PFDM) approach. Furthermore, the results were used to calibrate the material parameters needed for future more complex simulations.

PFDM simulations were performed to predict debonding of the matrix-particle interface in a spherical glass particle embedded in Sylgard. The simulations are performed using a 3D parallel software (Note: The code is available at <http://c-primed.github.io/fvm/>), MEMOSA, which is based on the cell-centered, finite-volume method [25]. The number of cells used in the simulations is 123,048 and they have an average size 20 μm . The particle matrix interface is defined as a region with twenty elements with length 2 μm in the radial direction. Details of the model and algorithm can be found in Xie et al. [26].

4. RESULTS AND DISCUSSION

4.1 Macroscale Thermomechanical Testing Results

Although the HTPB/ammonium chloride plate samples had been previously tested under ambient conditions in prior work, the tests were repeated in order to gather baseline data and quantify the impact of sample aging. The vibrometer-recorded H1 frequency response estimators for a representative plate sample in ambient conditions in response to three levels of excitation are presented in Figures 5-7 for the 50%, 65%, and 75% solids loading plates, respectively.

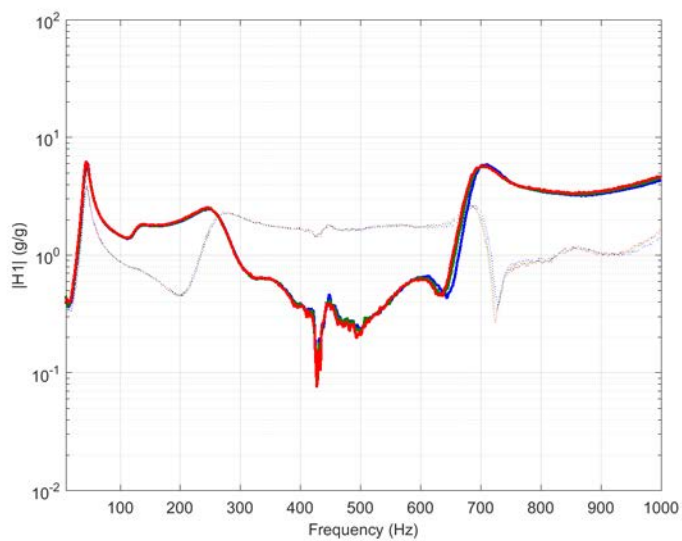


Figure 5. Experimental H1 mechanical frequency response estimator for a 50% solids loading plate obtained at three levels of excitation. The blue, green, and red curves depict responses at 1, 1.86, and 2.44 g RMS, respectively. Solid lines represent data from the geometric center, and dashed lines represent data from the offset point.

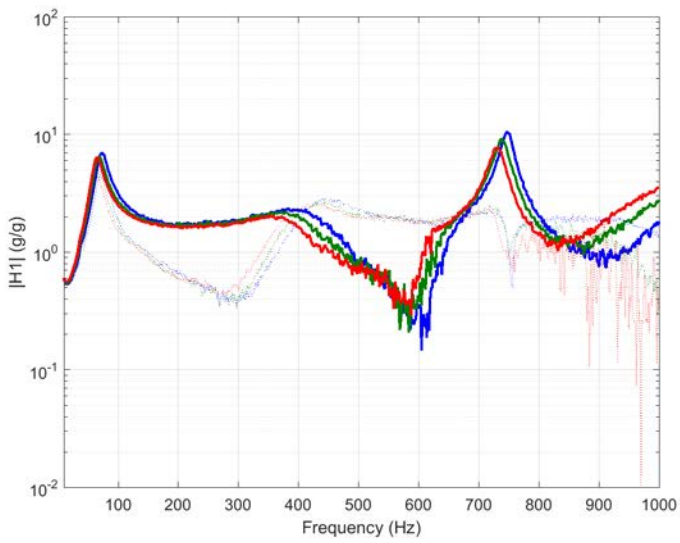


Figure 6. Experimental H1 mechanical frequency response estimator for a 65% solids loading plate obtained at three levels of excitation. The blue, green, and red curves depict responses at 1, 1.86, and 2.44 g RMS, respectively. Solid lines represent data from the geometric center, and dashed lines represent data from the offset point.

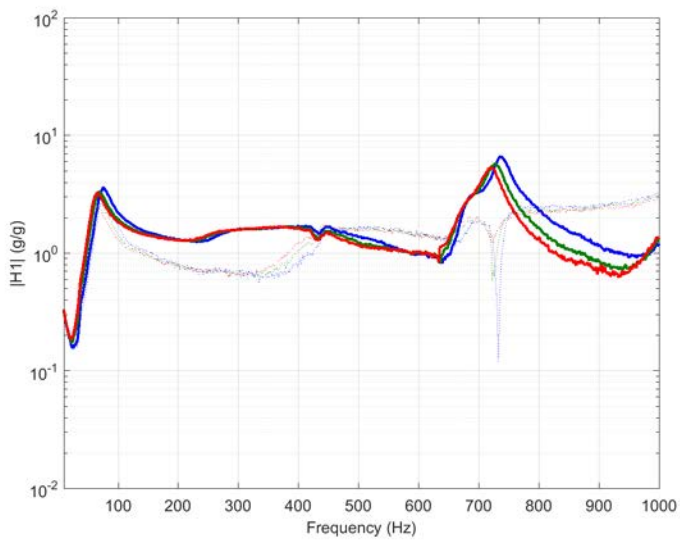


Figure 7. Experimental H1 mechanical frequency response estimator for a 75% solids loading plate obtained at three levels of excitation. The blue, green, and red curves depict responses at 1, 1.86, and 2.44 g RMS, respectively. Solid lines represent data from the geometric center, and dashed lines represent data from the offset point.

Concurrent with mechanical excitation and characterization, the thermal response for each of the plate samples was recorded using the aforementioned FLIR infrared camera. These experiments were performed over a 60 min time interval under a 2 g sinusoidal excitation near the first resonant frequency of each respective plate (where the highest heating is typically expected). The measured plate surface temperatures are plotted in Figures 8 and 9. The legend indicates the solids loading, followed by the sample number. The colored envelope surrounding each curve indicates one standard deviation for each trial.

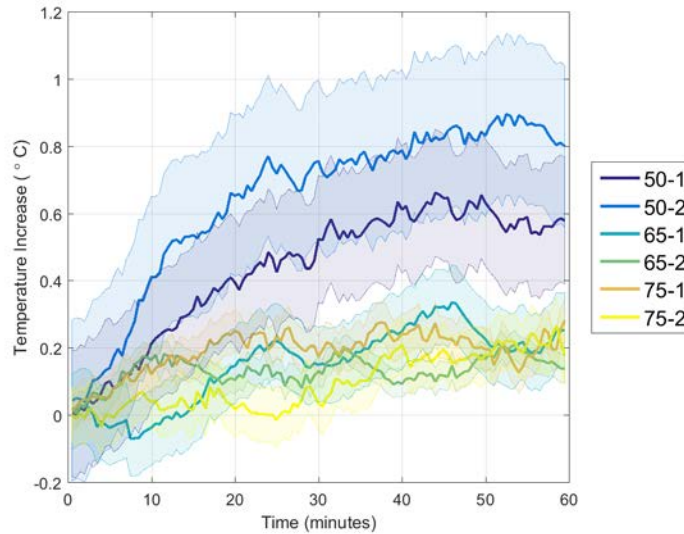


Figure 8. Experimentally-obtained mean plate surface temperature shown as a function of time

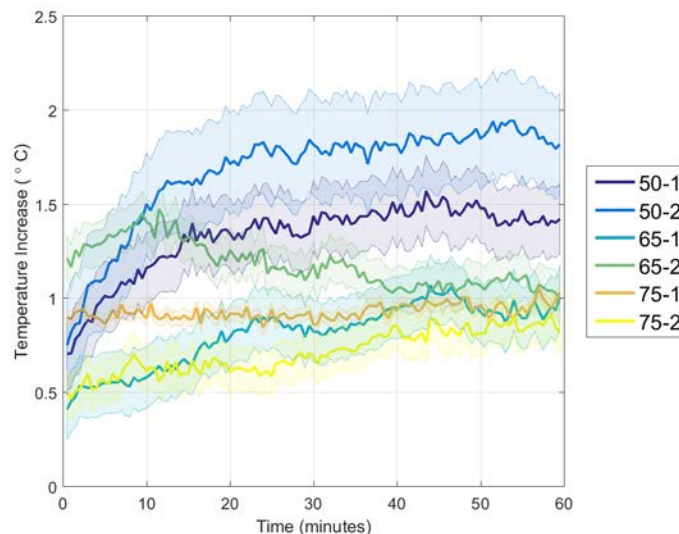


Figure 9. Experimentally-obtained maximum plate surface temperature shown as a function of time

In an effort to determine the influence of thermal boundary conditions on the temperature increase of the mock energetic plate samples when subjected to harmonic excitation, a thermally-insulated box was constructed to roughly simulate an insulated environment. The structural integrity of the box was maintained by acrylic panes with a 3.8 cm clearance relative to the top surface of the plate, and additional thermal insulation was provided by 1.9 cm thick foam insulation, which was attached on all sides. The box attached to the outside of the clamping fixture of the plate sample and moved with the shaker head during the course of experimentation.

Due to the nontransparent nature of the insulation box, the temperature profile as a function of time could not be obtained with the infrared thermal camera as before. As a result, the thermal camera was used to collect a snapshot of data at the beginning and end of the 60 min time interval and the mean and maximum temperature difference between these two instances was calculated. A similar calculation was performed on the ambient temperature profiles presented above to yield the values detailed in Table 3.

Table 3. A comparison of the experimentally-obtained plate surface temperature increases under insulated and ambient thermal boundary conditions in response to a 2 g excitation near the first resonant frequency for all of the plates

Solids Loading Sample	Mean Temperature Increase		Maximum Temperature Increase	
	Insulated	Ambient	Insulated	Ambient
50% - 1	1.8 °C	0.6 °C	2.5 °C	1.4 °C
50% - 2	1.6 °C	0.8 °C	2.1 °C	1.7 °C
65% - 1	1.2 °C	0.3 °C	1.5 °C	1.0 °C
65% - 2	1.0 °C	0.1 °C	1.6 °C	1.0 °C
75% - 1	2.1 °C	0.3 °C	2.5 °C	1.0 °C
75% - 2	1.9 °C	0.2 °C	2.3 °C	0.7 °C

As evident from the values provided above, the insulated boundary condition does result in a greater temperature increase in all of the cases as expected. *However, the observed trends appear to be inconsistent with simple bulk-scale heat transfer models.* Current efforts are focused on determining whether this is due to experimental error (i.e., measuring small temperature changes via an infrared camera), or directly attributable to the particulate composite nature of the material.

In order to determine an analytical (albeit conservative, due to the nature of the material) upper bound for the expected temperature increase under ambient and insulated conditions, a heat generation simulation was conducted in COMSOL using techniques detailed in prior work [4]. The mean and maximum temperature increases for the simulated plate are shown in Figures 10 and 11 for ambient and insulated boundary conditions. Simulations were performed on both 50% and 75% solids loading plate samples for the sake of comparison. It should be noted that though the temperature increases reported here are comparatively small (<10 °C), they can be exacerbated by local stress concentrations (a focus of Task Order 0002). In addition, recent work has demonstrated that this low-order heating (attributable to viscoelastic loss mechanisms) may be a strong indicator of a sample's probability of achieving thermal run-away and deflagration [27].

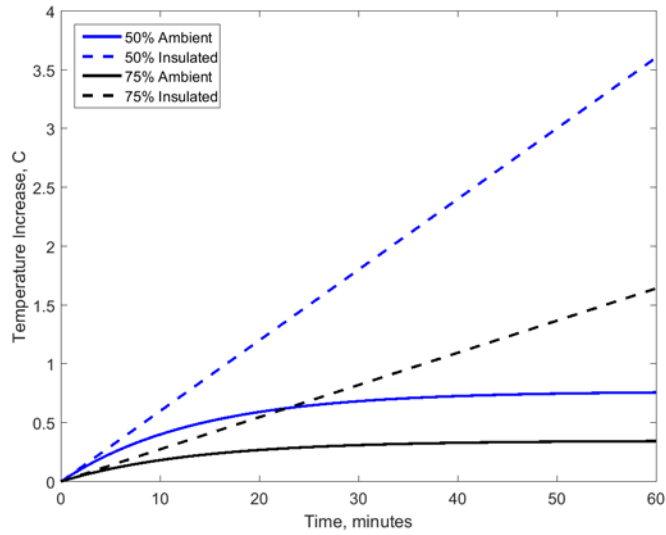


Figure 10. Simulated mean plate surface temperature shown as a function of time

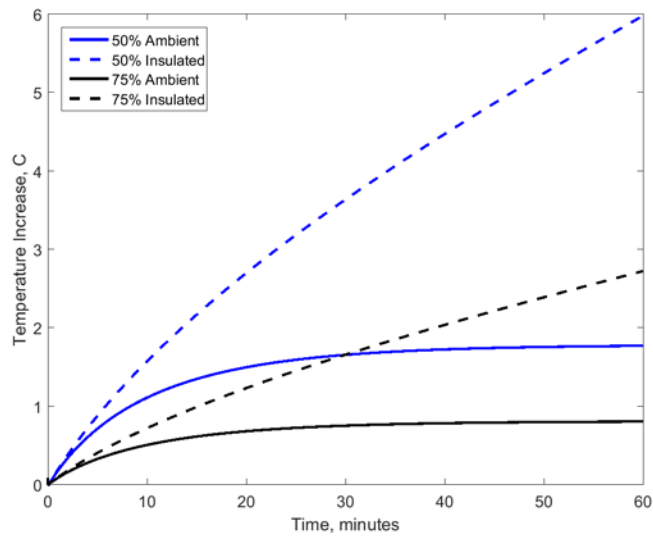


Figure 11. Simulated maximum plate surface temperature shown as a function of time

Experiments identical to the ambient thermal boundary condition tests described above were performed on plates of varying solids loading and additive content created as part of the PBXN-109 sample set. Note that the data presented below does not constitute the entire data set as there are an additional six plates to be fabricated and tested in coming months.

In order to minimize the effect of aging, all of the following plate samples were tested at an age of 43 days. The vibrometer-recorded H1 frequency response estimators for a representative plate in ambient conditions in response to three levels of excitation are presented in Figures 12 and 13 for the 85% solids loading plates with 0% and 30% additive content, respectively.

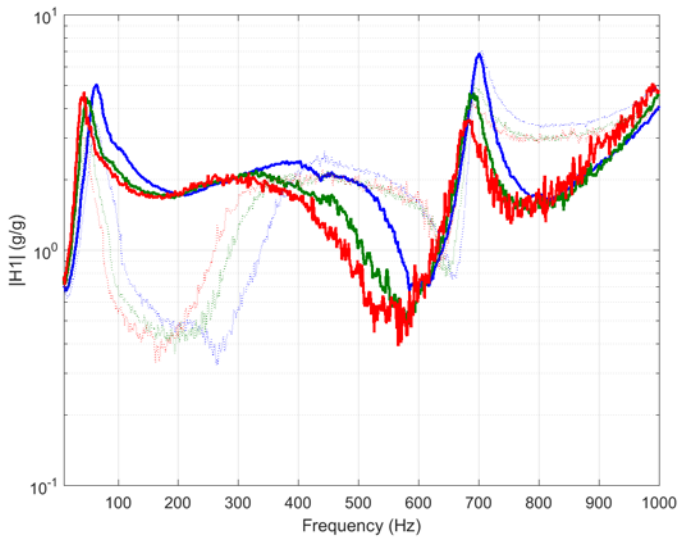


Figure 12. Experimental H1 mechanical frequency response estimator obtained for an 85% solids loading - 0% additive content plate at three levels of excitation. The blue, green, and red curves depict responses at 1, 1.86, and 2.44 g RMS, respectively. Solid lines represent data from the geometric center, and dashed lines represent data from the offset point.

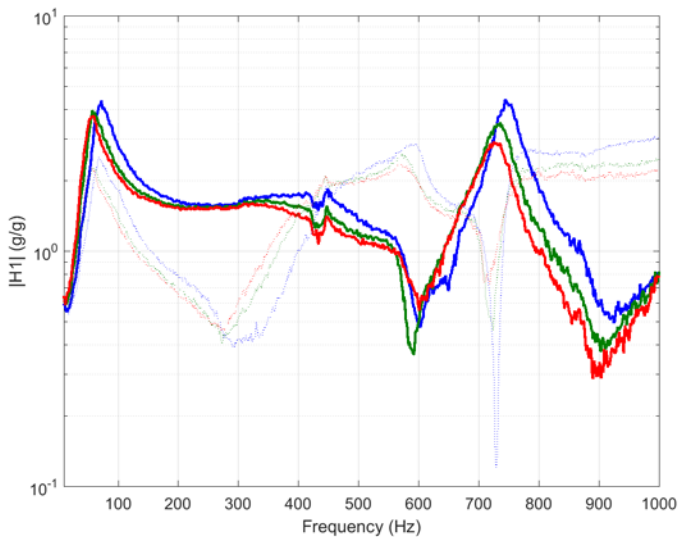


Figure 13. Experimental H1 mechanical frequency response estimator obtained for an 85% solids loading - 30% additive content plate at three levels of excitation. The blue, green, and red curves depict responses at 1, 1.86, and 2.44 g RMS, respectively. Solid lines represent data from the geometric center, and dashed lines represent data from the offset point.

As before, the corresponding thermal response for each of the plate samples was recorded using the FLIR infrared camera. This experiment was performed over a 60 min time interval under a

2 g sinusoidal excitation near the first resonant frequency of each respective plate. The plate surface temperatures are plotted in Figures 14 and 15. The legend indicates the solids loading content, followed by the additive content and the sample number. The colored envelope surrounding each curve indicates one standard deviation for each trial. Of particular note here is the non-trivial increase in the observed temperature rise in the presence of the metallic additive (aluminum).

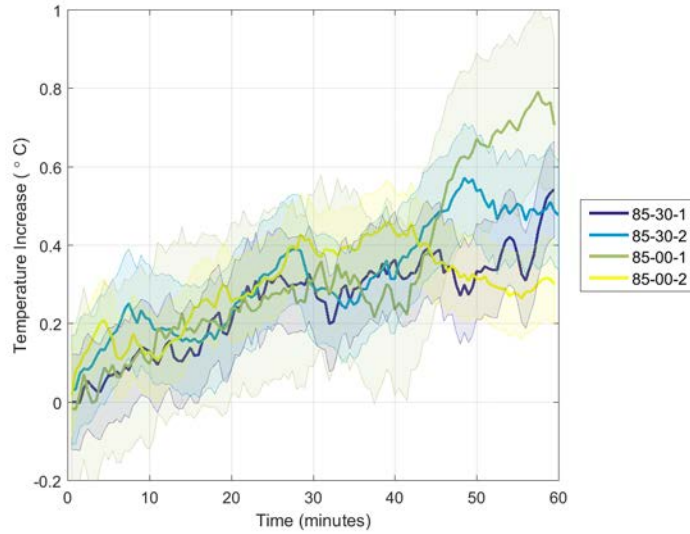


Figure 14. Experimentally-obtained mean plate surface temperature shown as a function of time

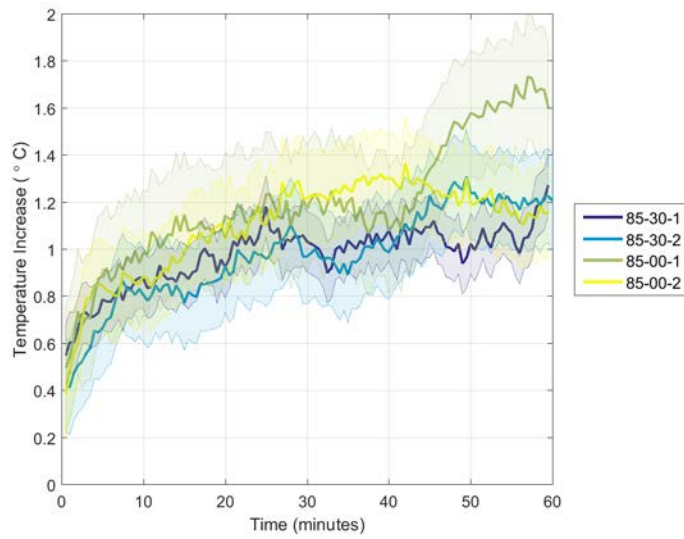


Figure 15. Experimentally-obtained maximum plate surface temperature shown as a function of time

4.2 Dissipative Modeling and Material Property Parameter Estimation

As alluded to above, a summary of the random base excitations testing conducted on the pure binder and high solids (85% solids where 100% of solids) loading sample are given in Figure A1 in the Appendix.

A sample result set from the testing on a 92-days-old, 76.2 mm (3 in) tall/diameter sample of the pure-binder PBXN-109 is shown in Figure 16. In this test, the base excitation was 2 g and the sweep was from 8 to 68 Hz in 60 s. This sample, which is much younger than the previously-tested pure-HTPB samples (only 92 days after fabrication) has stronger nonlinear behavior than was observed with the older, pure-HTPB samples which were more than 180 days old when tested. A spectrogram of the acceleration response of the mass is shown in Figure 16(a). There are clearly harmonics present in the response; the harmonic at twice the excitation frequency is prominent. A harmonic extraction process was developed to examine the envelope of the response at the driving frequency, and the results of applying this process are shown in Figure 16(b). Again, some evidence of quadratic nonlinearity is seen; there is an increase in response from the general trend lines at half the resonance frequency. This sample is much more lightly damped and softer than the older pure-HTPB samples. Estimates of the linear damping coefficient and Young's modulus were an order of magnitude lower than those for previously-tested, older pure-HTPB samples.

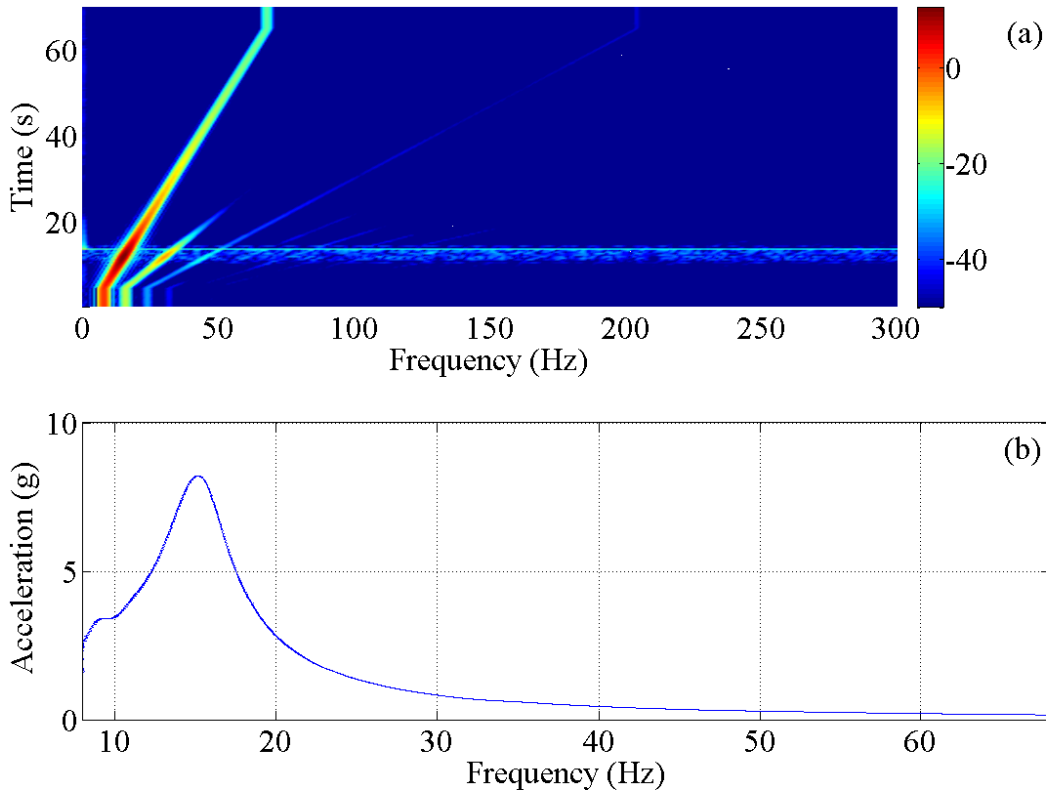


Figure 16. (a) A spectrogram of the response of the mass-material system undergoing swept sine excitation. (b) The response at the excitation frequency. The sample is a 76.2 mm (3 in) sample of HTPB with 0% solids loading excited at 2 g.

As an example, the results of fitting models to data from 3 swept sine tests on a 76.2 mm (3 in) cylinder of HTPB 50% are shown in Figure 17. In these tests, the sample weight was 0.4 kg and the mass loading was 0.98 kg. The models contain either a linear viscous or nonlinear hysteretic damping term, an N^{th} order nonlinear stiffness term, and a hereditary viscoelastic term, which is the convolution of a forcing function and a sum of exponentials kernel. Various types of viscoelastic models are considered, including those with different kernel orders and different forcing functions. The forcing is either: (a) a function of the relative velocity of the mass (directly related to strain rate); (b) a function of the nonlinear stiffness term (directly related to a nonlinear function of strain); or (c) a function of the hysteretic damping term. The model structures that were used to produce the results in Figure 17 are given in Table 4. The data used in the estimation of the model parameters were from three swept sine tests with excitation levels at 5 g, 7.5 g and 10 g.

Also shown in Figure 17 are the envelopes of the acceleration of the mass relative to the base when the mass-material system is undergoing a swept sine excitation at 5 g. Figure 17(b) is the part of Figure 17(a) near the primary resonance of the system (230 Hz – 270 Hz). The experimental relative acceleration signal envelope (blue) and the predicted envelopes from the estimated models: Models 1 (green), 4 (red), 6 (black) and 7 (purple) are shown. All of the models with the higher-order viscoelastic kernels perform better than Model 1 close to resonance, but Model 1 performs better well below resonance. In this region (160–180 Hz) Models 4 and 6 over-predict and Model 7 under-predicts the relative response levels. Above resonance, Model 6 under-predicts the experimental response envelope, whereas the responses of Models 4 and 7 are close to the experimental response envelope.

Table 4. Model numbers and corresponding model structure

Model Number	Stiffness Polynomial Order (N)	Damping Term $\dot{z} \dot{z} ^\lambda$	Viscoelastic Kernel Order (M)	Viscoelastic Forcing
1	5	Linear $\lambda = 0$	1	Type (a)
4	5	Linear $\lambda = 0$	20	Type (a)
6	5	Nonlinear $\lambda = 1.8$	20	Type (c)
7	5	Nonlinear $\lambda = 1.8$	20	Type (a)

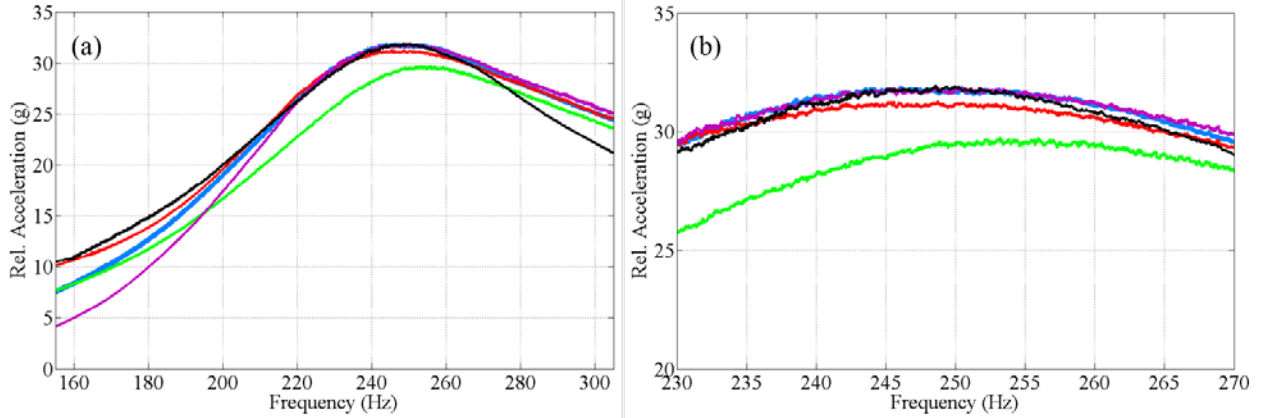
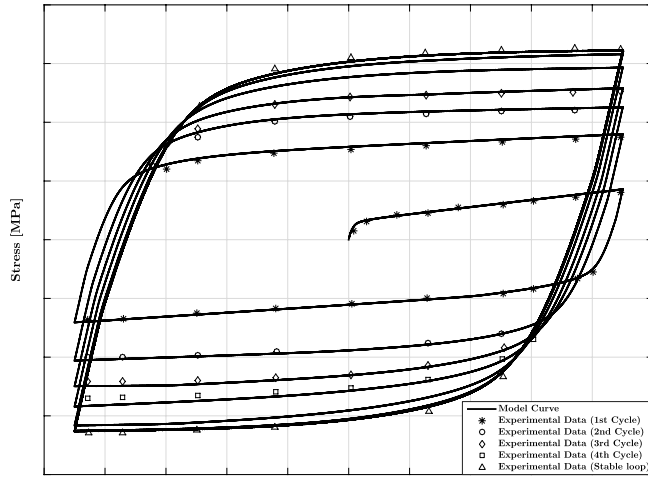


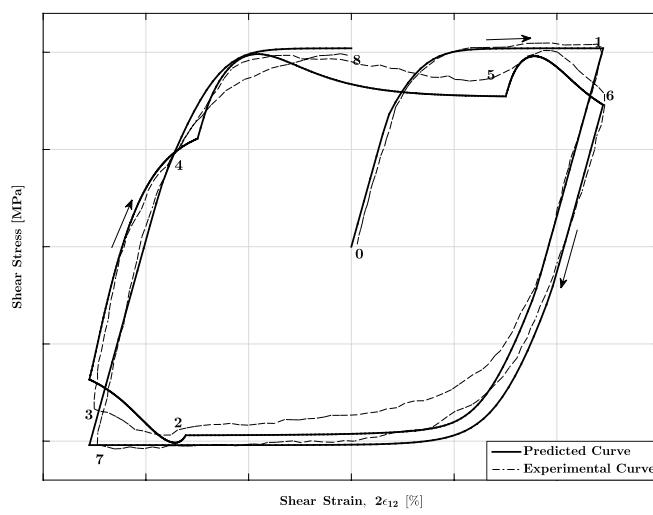
Figure 17. (a) The experimentally-obtained relative acceleration signal envelope (blue) and the predicted envelopes from the estimated models: Model 1 (green), 4 (red), 6 (black) and 7 (purple). (b) The information in sub-figure (a) expanded close to the resonance of the system. The sample here is HTPB with 50% solids loading excited at 5 g; estimation data: 3 swept sine tests at 5 g, 7.5 g and 10 g base excitation levels.

4.3 Endochronic Plasticity Model Results

The 3D endochronic numerical implementation (detailed in depth in the Appendix) was used to model the loading behavior of OFHC copper, and the model results were compared with experimental results reported by Lamba and Sidebottom [28,29]. The kernel and hardening parameters were calibrated using the uni-axial, constant strain amplitude, cyclic loading experimental data reported in [28]. Figure 18(a) shows the prediction of stress-strain response of OFHC copper under a uni-axial constant strain amplitude cyclic loading, while Figure 18(b) shows the prediction of the shear stress-strain response of OFHC copper subjected to a biaxial loading, both compared with experimental results. The prediction of uniaxial cyclic loading in Figure 18(a) is extremely accurate, thus verifying our calibration procedure and numerical implementation, since the model parameters were calibrated directly from uniaxial cyclic loading data. The prediction of shear stress-strain response in Figure 18(b), though not completely accurate, gives a good representation of the experimental measurements, thus validating our calibration procedure and numerical implementation.



(a)



(b)

Figure 18. (a) Uniaxial constant strain amplitude cyclic hardening response of OFHC copper [endochronic model (solid line) vs experimental data (symbols)]. (b) Prediction of the shear stress versus shear strain of biaxial non-proportional loading of the OFHC copper [endochronic model (solid line) vs experimental data (dashed line)].

4.4 Crystal-Binder Interface Results

The elastic constants of the glass bead used in the aforementioned phase field simulations are listed in Table 5. To choose the elastic constants for Sylgard, quasistatic loading simulations were performed and compared to the first deformation stages of the experimental force displacement curve shown Figure 19. The best fit occurs for $E = 75$ MPa.

Table 5. The elastic constants for Sylgard and glass used in the simulations

	Sylgard 184	Glass bead
E	75 MPa	70 GPa [30]
v	0.44 [31]	0.3

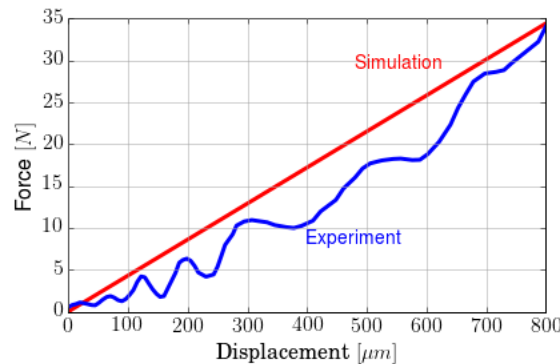


Figure 19. Force displacement curves used for the calibration of the elastic constant of Sylgard. The experiments were performed by the Son and Chen groups at Purdue University.

Figure 20 shows the simulated damage field. A larger amount of damage is observed in xz plane due to the asymmetry of the dimensions of the sample. Figure 21 shows the delaminated region in the experiments and in the simulations for an applied displacement of 624 μm .

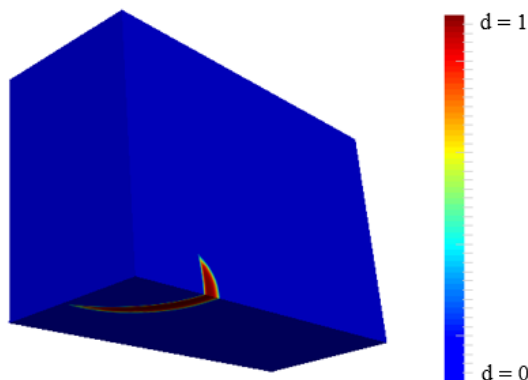


Figure 20. A contour plot of the damage field for an applied displacement of 800 μm displacement on top of the domain

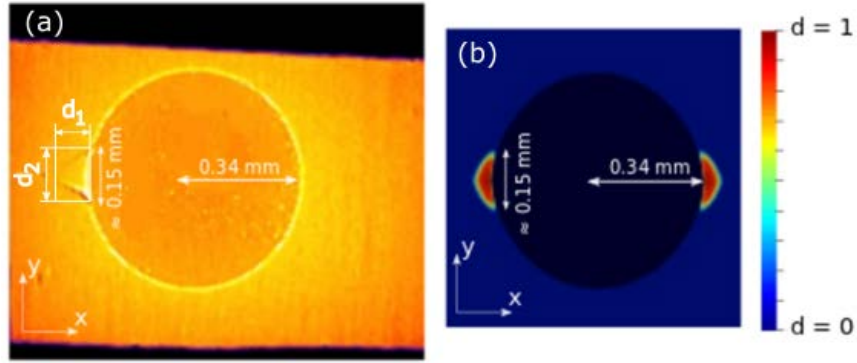


Figure 21. (a) Experiment and (b) simulation of debonding for a 624 μm displacement applied vertically

5. CONCLUSIONS

The research described herein has advanced the understanding of the near-resonant response of energetic materials to periodic loading through a joint analytical, numerical, and experimental investigation. The refined modeling tools developed with this improvement in basic understanding are currently being distilled and transferred to the Air Force Research Laboratory for Department of Defense use. Despite what are believed to be positive advancements, considerable work remains. In particular, additional research focus is warranted for systems with macroscopic geometric discontinuities/stress concentrations (e.g., cracks, steps in geometry, and intentional holes), alternate sample geometries, and less traditional binder systems (e.g., those with a high degree of compliance or the converse) than those considered here. In addition, there is a need for continued development of the endochronic material model, preliminary experimental validation of this model, and an exploration of how this model can be mathematically coupled with viscoelastic models. Finally, efforts should be made to distill lessons learned from crystal-scale computational models into structural-scale models via "effective material properties" or an alternate multi-scale approach.

6. REFERENCES

1. J. O. Mares, J. K. Miller, N. D. Sharp, D. S. Moore, D. E. Adams, L. J. Groven, J. F. Rhoads, and S. F. Son. Thermal and mechanical response of PBX 9501 under contact excitation. *Journal of Applied Physics*. 2013. **113**(8): 084904.
2. J. O. Mares, J. K. Miller, I. E. Gunduz, J. F. Rhoads, and S. F. Son. Heat generation in an elastic binder system with embedded discrete energetic particles due to high-frequency, periodic mechanical excitation. *Journal of Applied Physics*. 2014. **116**(20): 204902.
3. J. K. Miller, D. C. Woods, and J. F. Rhoads. Thermal and mechanical response of particulate composite plates under inertial excitation. *Journal of Applied Physics*. 2014. **116**(24): 244904.
4. D. C. Woods, J. K. Miller, and J. F. Rhoads. On the thermomechanical response of HTPB-based composite beams under near-resonant excitation. *Journal of Vibration and Acoustics*. 2015. **137**(5): 054502.

5. J. K. Miller, J. O. Mares, I. E. Gunduz, S. F. Son, and J. F. Rhoads. The impact of crystal morphology on the thermal responses of ultrasonically-excited energetic materials. *Journal of Applied Physics*. 2016. **119**(2): 024903.
6. J. Paripovic. Characterization and modeling of materials used in improvised explosive devices. M. S. Thesis. 2013. Purdue University.
7. N. P. Loginov, S. M. Muratov, and N. K. Nazarov. Initiation of Explosion and Kinetics of Explosive Decomposition Under Vibration [Translated]. *Combustion, Explosion, and Shock Waves*. 1976. **12**(3), p. 367-370.
8. N. P. Loginov. Structural and physicochemical changes in RDX under vibration. *Combustion, Explosion, and Shock Waves*. 1997. **33**(5), p. 598-604.
9. J. E. Field. Hot Spot Ignition Mechanisms for Explosives. *Accounts of Chemical Research*. 1992. **25**(11): p. 489-496.
10. B. L. Hamshere, I. J. Lockert, R. M. Dexter. Evaluation of PBXN-109: the explosive fill for the Penguin 12 anti-ship missile warhead. Systems Science Laboratory, Defense Science and Technology Organization. 2003. DSTO-TR-1471.
11. K. Valanis. A theory of viscoplasticity without a yield surface. *Archives of Mechanics*. 1971. **23**: p. 517–533.
12. K. C. Valanis and C. F. Lee. Endochronic theory of cyclic plasticity with applications. *Journal of Applied Mechanics*. 1984. **51**(2): p. 367–374.
13. N. K. Kucher and M. V. Borodii. Version of the endochronic theory of plasticity for describing complicated cyclic loading histories. *Strength of Materials*. 1993. **25**(5): p. 315–322.
14. Z. P. Bazant and P. D. Bath. Endochronic theory of inelasticity and failure of concrete. *Journal of the Engineering Mechanics Division*. 1976. **102**(4): p. 701–722.
15. Z. P. Bazant and R. J. Krizek. Endochronic constitutive law for liquefaction of sand. *Journal of the Engineering Mechanics Division*. 1976. **102**(2): p. 225–238.
16. G. M. Owolabi and M. N. K. Singh. Experimental evaluation of two multiphase constitutive models applicable to metal matrix composites under nonproportional variable amplitude loading. *Journal of Mechanics of Materials and Structures*. 2007. **2**(1): p. 131–148.
17. C. Netzeker, H. Dal and M. Kaliske. An endochronic plasticity formulation for filled rubber. *International Journal of Solids and Structures*. 2010. **47**(18-19): p. 2371–2379.
18. C. Zopf, M. A. Garcia, and M. Kaliske. A continuum mechanics approach to model asphalt. *International Journal of Pavement Engineering*. 2014. **16**(2): p. 105–124.
19. S. Y. Hsu, S. K. Jain, and O. H. Griffin. Verification of endochronic theory for non-proportional loading paths. *ASCE Journal of Engineering Mechanics*. 1991. **117**(1): p. 110–131.
20. M. Ortiz and A. Pandolfi. Finite-deformation irreversible cohesive elements for three-dimensional crack-propagation analysis. *International Journal for Numerical Methods in Engineering*. 1999. **44**(9): p. 1267–1282.
21. T. Siegmund, N. A. Fleck, and A. Needleman. Dynamic crack growth across an interface. *International Journal of Fracture*. 1997. **85**(4): p. 381–402.
22. K. Matous, M. G. Kulkarni, and P. H. Geubelle. Multiscale cohesive failure modeling of heterogeneous adhesives. *Journal of the Mechanics and Physics of Solids*. 2008. **56**(4): p. 1511–1533.

23. C. Miehe, H. Dal, L. M. Schanzel, and A. Raine. A phase-field model for chemo-mechanical induced fracture in lithium-ion battery electrode particles. *International Journal For Numerical Methods In Engineering*. 2015. **106**(9): p. 683–711.
24. H. Amor, J.-J. Marigo, and C. Maurini. Regularized formulation of the variational brittle fracture with unilateral contact: Numerical experiments. *Journal of the Mechanics and Physics of Solids*. 2009. **57**(8): p. 1209–1229.
25. S. Das, S. R. Mathur, and J. Y. Murthy. An unstructured finite-volume method for structure–electrostatics interactions in MEMS. *Numerical Heat Transfer, Part B: Fundamentals*. 2011. **60**(6): p. 425–451
26. Y. Xie, O. G. Kravchenko, R. B. Pipes, and M. Koslowski. Phase field modeling of damage in glassy polymers. *Journal of the Mechanics and Physics of Solids*. 2016. **93**: 182–197.
27. J. O. Mares. Thermal and Mechanical Response of PBX 9501 and Simulants Under High Frequency Contact Excitation. Ph.D. Dissertation. 2016. Purdue University.
28. H. S. Lamba and O. M. Sidebottom. Proportional biaxial cyclic hardening of annealed oxygen-free high-conductivity copper. *Journal of Testing and Evaluation*. 1978. **6**(4): p. 260–267.
29. H. S. Lamba and O. M. Sidebottom. Cyclic plasticity for nonproportional paths: Part 2 – comparison with predictions of three incremental plasticity models. *Journal of Engineering Materials and Technology*. 1978. **100**(1): p. 104–111.
30. I. Agnolin and J. N. Roux. Sound wave velocities in dry and lubricated granular packings: Numerical simulations and experiments. *Optical Coherence Tomography in Cardiovascular Research*. 2007. p. 313-316.
31. I. D. Johnston, D. K. McCluskey, C. K. L. Tan, and M. C. Tracey. Mechanical characterization of bulk Sylgard 184 for microfluidics and microengineering. *Journal of Micromechanics and Microengineering*. 2014. **24**(3): p. 035017.

LIST OF FIGURES IN THE APPENDIX

Figure		Page
A1	A summary of a random base excitation test lasting for 100 s from 10 Hz to 1000 Hz at 0.050 g ² /Hz for sample P85 S100 Q00 C03.	30
A2	Experimental test setup with surrogate sample and a graphical representation of the mass-material system.	31
A3	The steps in the iterative system identification approach used for parameter estimation. The black outlined boxes illustrate the initialization of the estimation, and the blue outlined boxes are the core of the iterative estimation scheme.	38
A4	The impulse response of a pure-HTPB sample (blue) excited at 5 g along with the predicted Prony approximation for (left) $M_1 = 250$ (red) and (right) the top energy contributing terms, $M = 10$ (green).	41
A5	The viscoelastic kernel frequency response magnitudes ($ vFRF $) derived from experiments on pure-HTPB excited at 10 g. The gray region denotes the region of strong excitation in the experiment, red is $ vFRF $ derived as part of the iterative whole model estimation process, blue is the region used in the $vFRF$ estimation process, and green is the $ vFRF $ predicted using the estimated viscoelastic kernel model when fitting $M_1 = 40$ and selecting only the top 10 terms. The regions used in estimation: (a) 50-110 Hz, and (b) 30-130 Hz.	43
A6	Flowchart of the algorithm used for the endochronic numerical implementation.	49
A7	The staggered algorithm used for the simultaneous calibration of the endochronic kernel and hardening functions.	52

LIST OF TABLES IN THE APPENDIX

Table	Page	
A1	Summary of the experimental testing status of the PBXN-109 samples. Here, F denotes Fracture, and Day 0 corresponds to the sample cure date. Each sample has its own number.	29
A2	All of the stiffness, damping and viscoelastic term combinations considered when fitting the mass material model to the simulated responses and experimental data from the sweep and random base excitation testing on HTPB surrogate samples.	33

A1. PERSONNEL

Name	Title	Project Role
Jeffrey F. Rhoads	Professor	PI
Steven F. Son	Professor	Co-PI
Patricia Davies	Professor	Co-PI
Marcial Gonzalez	Assistant Professor	Co-PI
Marisol Koslowski	Associate Professor	Co-PI
Brandon Terry	Post-Doctoral Researcher	Sample preparation
Allison Range	Graduate Research Assistant	Sample preparation and thermomechanical characterization
Jelena Paripovic	Graduate Research Assistant	Dissipative modeling and system identification
Ankit Agarwal	Graduate Research Assistant	Endochronic plasticity modelling
Johanna Palsdottir	Graduate Research Assistant	Interface modeling
Bogdan Tanasoiu	Graduate Research Assistant	Interface modeling
Camilo Cordon	Graduate Research Assistant	Interface modeling
Jaylon Tucker	Undergraduate Research Assistant	Sample preparation and thermomechanical characterization

A2. Publications and Presentations

List of Publication

- Nothing to report for this performance period

List of Presentations

1. J. Paripovic, A. Range, J. Tucker, and P. Davies. Sample size effects when determining mechanical properties of surrogate energetic materials from low frequency base excitation tests. IMECE 2016: The 2016 ASME International Mechanical Engineering Congress and Exposition. 2016. Phoenix, Arizona.
2. M. Koslowski, Y. Xie, J. Palsdottir, and B. Tanasoiu. Modeling dynamic fracture in PBX: A phase-field model. IMECE 2016: The 2016 ASME International Mechanical Engineering Congress and Exposition. 2016. Phoenix, Arizona.

A3. Test Schedule and Test Reports

The information in this appendix relates to material in Sections 3.3 and 4.2 of this report. It contains the base excitation material testing schedule and an example of a testing summary report for a random base excitation test. These types of reports are automatically generated when a test is completed and they serve as a record of the test. The format for a swept sine test summary is under revision because in recent tests responses have included much stronger harmonic content than previously seen (Note: we are now testing much younger samples than previously utilized, as well as a slightly different composition) and we would like to capture that information in the test report.

The geometry, composition, and cure date of the samples being tested along with the testing progress is shown in Table A1. The testing matrix is divided into harmonic and random base excitation testing. For the 76.2 mm (3 in.) tall/diameter high solids loading sample (85% solids loading where 70% of solids is sucrose and the remaining 30% is the aluminum additive). When a series of 10 scheduled tests is terminated due to the fracturing of a sample, that is denoted by F. After the initial 10 scheduled harmonic and random tests per samples are completed, we will continue tests based on the experimental results to further understand the dynamic behavior of the samples.

A summary report of a random base excitation test is shown in Figure A1. The report contains the geometry of the sample, testing conditions, base excitation, and response of the signal, as well as the power spectral densities and the magnitude and phase of the estimated frequency response function relating the base acceleration to the relative acceleration of the mass. The estimated coherence is also shown. The frequency response estimates for the random excitation tests are estimated by using the H1 estimator and the cross and power spectral density estimates are estimated by using segment averaging. In the segment averaging a Hann window was used, segments overlapped by 50% and they were 8192 points long, giving, with a sample rate of 6000 samples/s, and a frequency resolution of just under 1 Hz. Results from 146 segments are averaged in the estimation.

Table A1. Summary of the experimental testing status of the PBXN-109 samples. Here, F denotes Fracture, and Day 0 corresponds to the sample cure date. Each sample has its own number.

Sample ID	Random Base Excitation			Harmonic Base Excitation				Completed/ Total Planned F	
	0.015 (g ² /Hz)	0.025 (g ² /Hz)	0.050 (g ² /Hz)	Completed/ Total Planned F	1g	2g	3g	4g	
	(Day #, Day #, ...)				(Day #, Day #, ...)				
P00_Q000_Q00_C01 HTPB 100% Solids 0% Diam: 1" Height: 1" Cure Date: 2/29/2016			77,86 ^F	2/10 F		77		77	2/10 F
P00_Q000_Q00_C02 HTPB 100% Solids 0% Diam: 1" Height: 1" Cure Date: 2/29/2016		86,102	86,102	4/10 F	109	109 ^F			2/10 F
P00_Q000_Q00_C03 HTPB 100% Solids 0% Diam: 3" Height: 3" Cure Date: 3/15/2016		84,123	84,123	4/10		85,92,99	92	85	5/10
P00_Q000_Q00_C04 HTPB 100% Solids 0% Diam: 3" Height: 3" Cure Date: 3/28/2016	78	64,78	78	4/10		79,86	79,86	79	5/10
P00_Q000_Q00_C05 HTPB 100% Solids 0% Diam: 1" Height: 1" Cure Date: 6/20/2016		4,25	4,25	4/10					0/10
P85_S070_A30_C03 HTPB 15% Solids 85% Diam: 3" Height: 3" Cure Date: 6/13/2016		15,29,36	15,29,36	6/10					0/10
P85_S100_A00_C03 HTPB 15% Solids 85% Diam: 3" Height: 3" Cure Date: 7/5/2016		15	15	2/10					0/10

Note: Sample IDs are defined by: A##_B###_C##_D##. A## specifies the binder formulation and overall solids loading (% of solid in overall formulation). For example, P designates that the binder is HTPB prepared as in a PBXN-109 propellant. B### specifies the type of mock energetic crystal and percentage of solids that are mock energetic (i.e., S100 means all solids are sucrose). C## gives the type of additive material and percentage of solids that are additive. Here, A designates Aluminum. D## gives the geometry and sample identification number. Here, C designates a cylinder. The Q designation followed by zeroes in any place essentially indicates that the metric is not applicable.

July 20, 2016 HTPB 85% PBXN-109 C03 Random Excitation at 0.025g²/Hz : test 1
 Date Cured: July 5, 2016 Age: 15 days
 Sample ID: P85 S100 Q00 C03

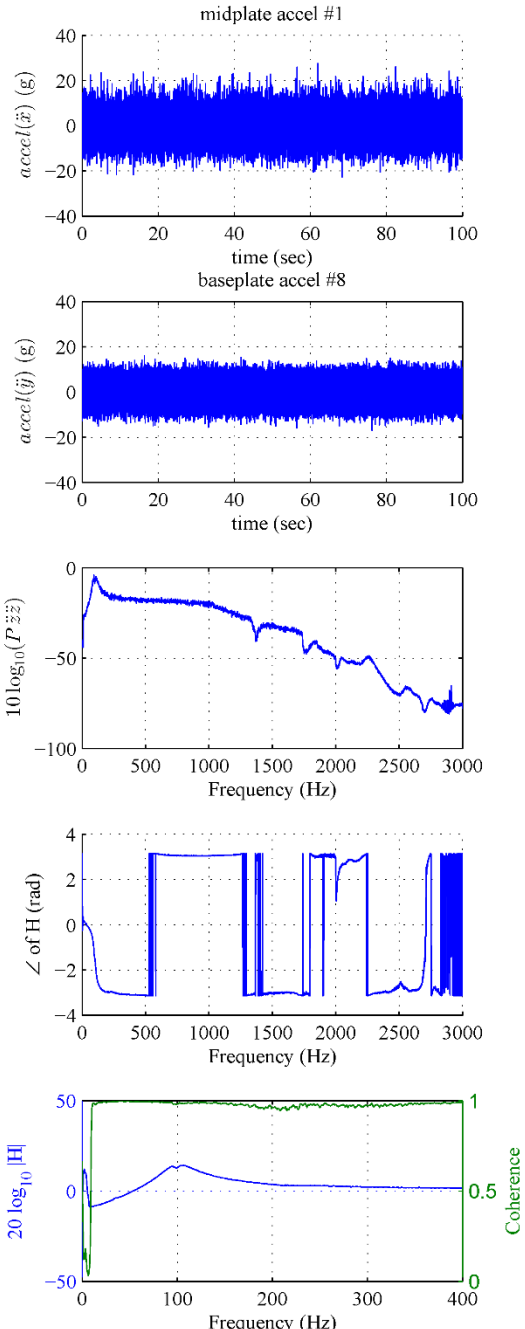
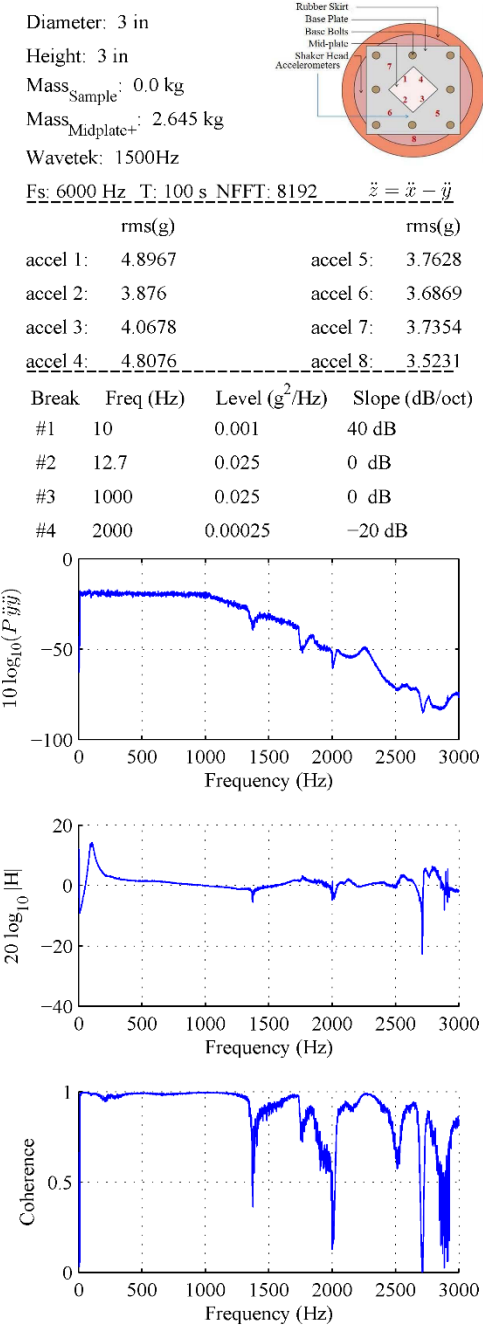


Figure A1. A summary of a random base excitation test lasting for 100 s from 10 Hz to 1000 Hz at 0.050 g²/Hz for sample P85 S100 Q00 C03

A4. Modeling and System Identification

An overview of the mass-material system model structure and the techniques used to estimate the model parameters are given in this appendix. The mass-material system that is being used in the experimental tests is modeled as a mass-spring-damper with a viscoelastic element. Motion is constrained to be in the vertical direction, and the base excitation to the system is provided by a shaker. The experimental apparatus and a graphical representation of the system model are shown in Figures A2.

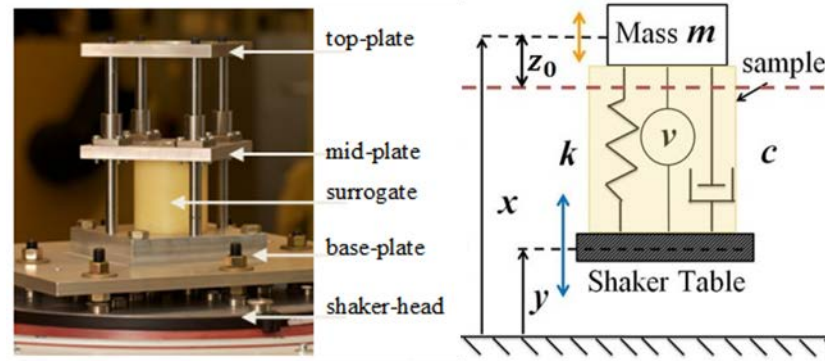


Figure A2. Experimental test setup with surrogate sample and a graphical representation of the mass-material system

A4.1. Model Structure

With reference to Figure A2, the equation of motion of the mass relative to the base is:

$$m\ddot{z}_1 + c'(\dot{z}_1, z_1) + k'(z_1) + v_1(f(z_1, \dot{z}_1)) = -m\ddot{y} - mg \quad (\text{A1})$$

where m is the mass, which is one-third of the mass of the material plus the mass of the center plate and any masses attached to it. $z_1 = x - y$ is the relative displacement of the attached mass, $k'(z_1)$ is the stiffness term, $c'(z_1, \dot{z}_1)$ is the damping term, $v_1(f(z_1, \dot{z}_1))$ is the viscoelastic term, and \ddot{y} is the base acceleration. This equation can be expanded about the static settling point z_0 and expressed in terms of the motion about this settling point: $z_1 = z_0 + z$. Noting also that $c'(0, z_0) + k'(z_0) + v_1(f(z_0, 0)) = -mg$ results in an equation about the settling point of the form:

$$m\ddot{z} + c(\dot{z}, z) + k(z) + v_1(f(z, \dot{z})) = -m\ddot{y} \quad (\text{A2})$$

The parameters in this equation are functions of the static settling point. Thus, to extract material parameters from estimates of the parameters of this equation requires knowledge of: (a) the static settling point, (b) the relationships between the terms in Equation A1 and the terms in Equation A2, and (c) the relationship between the parameters in Equation A1 and the parameters of the corresponding stress-strain form of that equation. In this appendix, the focus is on describing

techniques to estimate the parameters of Equation A2, but it is noted that several additional steps are required to translate those estimates into material parameters.

Many different forms of the damping, stiffness, and viscoelastic terms are considered in the modeling process. The terms may depend on the relative velocity (\dot{z}), the relative displacement (z), or a combination of both. From linear viscous damping ($c\dot{z}$) and linear stiffness (kz), to more complex expressions, such as so-called hysteretic damping terms of the form $(c\dot{z}|\dot{z}|^\lambda)$. When considering nonlinear stiffness models, an N th order polynomial expression in z ($\sum_{i=1}^N k_i z^i$) is used because it is linear in parameters. Use of Ogden's hyperelastic model has been explored previously [A1, A2] and Paripovic and Widdle both showed that an Ogden model can be fitted to the estimated polynomial stiffness term to extract hyperelastic material parameters. For the viscoelastic term, a hereditary model was chosen. The general form of this model is a convolution of a hereditary (sum of exponentials) kernel and a forcing function:

$$v(t) = f(z, \dot{z}) * g(t) = \int_{-\infty}^t f(z(\tau), \dot{z}(\tau)) g(t - \tau) d\tau \quad (A3)$$

where $g(t)$ is the relaxation kernel, $f(z, \dot{z})$ is an arbitrary driving function that may depend on the relative displacement, relative velocity or both. The relaxation kernel, $g(t)$ is of the form:

$$g(t) = \sum_{i=1}^M \beta_i e^{-\alpha_i t} \quad (A4)$$

where M is the order of the viscoelastic model, and α_i and β_i are the viscoelastic model parameters. Combining Equations A3 and A4 gives:

$$v(t) = f(z, \dot{z}) * g(t) = \int_{-\infty}^t f(z(\tau), \dot{z}(\tau)) \sum_{i=1}^M \beta_i e^{-\alpha_i(t-\tau)} d\tau \quad (A5)$$

When modeling the dynamic behavior of the HTPB samples, first, the linear case was considered with no viscoelastic term and then terms were systematically added and/or adapted to improve the accuracy of the model predictions. The various model structures that have been examined so far are shown in Table A2.

Table A2. All of the stiffness, damping and viscoelastic term combinations considered when fitting the mass material model to the simulated responses and experimental data from the sweep and random base excitation testing on HTPB surrogate samples

Model	Stiffness $k(z)$	Damping $c(\dot{z})$	Viscoelastic Term $f(z, \dot{z})$	Kernel Order M
1	$k_1 z$	$c \dot{z}$	-	-
2	$\sum_{i=1}^5 k_i z^i$	$c \dot{z}$	-	-
3	$\sum_{i=1}^5 k_i z^i$	$c \dot{z} \dot{z} ^\lambda$	-	-
4(a)	$\sum_{i=1}^5 k_i z^i$	$c \dot{z}$	$z(t)$	1
4(b)	$\sum_{i=1}^5 k_i z^i$	$c \dot{z}$	$\dot{z}(t)$	various
5	$\sum_{i=1}^5 k_i z^i$	$c \dot{z}$	$\sum_{i=1}^5 k_i z^i$	1
6	$\sum_{i=1}^5 k_i z^i$	$c \dot{z} \dot{z} ^\lambda$	$\dot{z} \dot{z} ^\lambda$	various
7	$\sum_{i=1}^5 k_i z^i$	$c \dot{z} \dot{z} ^\lambda$	$\dot{z}(t)$	various

A4.2. Model Parameter Estimation for Low Order Viscoelastic Models

In [3] Paripovic focused on models with no viscoelastic term ($v = 0$) or with a viscoelastic kernel of order 1 ($M = 1$). The estimation technique used for these cases was continuous-time system identification. When viscoelastic kernels are higher order, the method described in this section becomes difficult to use, and so an iterative parameter estimation technique was developed for when $M > 2$; that technique is described in a later section. The iterative method also utilizes continuous-time estimation to estimate the stiffness and damping model parameters.

A4.2.1. Continuous-Time System Identification Approach

The continuous-time system identification methodology is introduced with its application to Model 2, where a linear viscous damping term, a 5th order polynomial stiffness, and $v(t) = 0$ is considered. The equation for Model 2 is:

$$m \ddot{z} + c \dot{z} + k_1 z^1 + k_2 z^2 + k_3 z^3 + k_4 z^4 + k_5 z^5 = -m \ddot{y} \quad (\text{A6})$$

Note that Equation A6, while nonlinear in z , is linear in parameters (k_i and c). The mass m is known, it is a sum of the mass of the midplate (0.98 kg), the thin aluminum plate that is glued to the sample, one third of the test specimens mass, and any additional mass fixed to the midplate.

Moving all of the known quantities to the right hand side and using the time histories samples, Equation A6 may be written as a system of equations of the form:

$$\begin{bmatrix} -m(\ddot{z}(\Delta) + \ddot{y}(\Delta)) \\ -m(\ddot{z}(2\Delta) + \ddot{y}(2\Delta)) \\ \vdots \\ -m(\ddot{z}(N\Delta) + \ddot{y}(N\Delta)) \end{bmatrix} = \begin{bmatrix} \dot{z}(\Delta) & z(\Delta) & z^2(\Delta) & \dots & z^5(\Delta) \\ \dot{z}(2\Delta) & z(2\Delta) & z^2(2\Delta) & \dots & z^5(2\Delta) \\ \vdots & \vdots & \vdots & \vdots & \vdots \\ \dot{z}(N\Delta) & z(N\Delta) & z^2(N\Delta) & \dots & z^5(N\Delta) \end{bmatrix} \begin{bmatrix} c \\ k_1 \\ k_2 \\ k_3 \\ k_4 \\ k_5 \end{bmatrix}$$

This can be expressed as:

$$\mathbf{q} = [\mathbf{A}]\mathbf{p} \quad (\text{A7})$$

where Δ is the time step in seconds. Note that each row in \mathbf{A} and \mathbf{q} is time aligned [A4]. Here, \mathbf{A} and \mathbf{q} are known since the experimental signals are measured and can be manipulated and conditioned appropriately to yield z^2 , z^3 , etc. \mathbf{p} is the vector of the unknown terms. One advantage of this method is that the time domain signals may be equally cropped to focus on a specific region of the response and avoid unwanted transient or noise corrupted portions of the signal. Solving the normal equations:

$$\{\mathbf{A}^T \mathbf{q}\} = [\mathbf{A}^T \mathbf{A}] \hat{\mathbf{p}} \quad (\text{A8})$$

where \mathbf{T} denotes transpose, yields an estimate of the parameter vector \mathbf{p} . This can be solved, for example, by using the *regress* command in MATLAB, which also provides confidence intervals and statistics related to the fit.

A4.2.2. Signal Processing

Before applying this approach to the measured experimental signals the signals must be appropriately filtered and conditioned to reduce ill-conditioning of the matrices which can impact the accuracy of the parameter estimates.

One challenge of applying this approach to experimental measurements is deriving the necessary velocity, displacement, and other higher order state space signals from the measured relative acceleration (\ddot{z}). One must be careful to condition the signal appropriately to avoid high levels of noise corruption on the signals. Also, care must be taken to make sure that all of the columns of the estimation matrix contain time histories that are equally filtered. For example, when deriving estimates of the velocity and displacement signals from the measured acceleration, the following process is used. First, the measured relative acceleration signal is passed through a Butterworth high pass filter with a cut-off frequency and roll-off rate chosen by considering the excitation range and the response characteristics of the system. The signal is then integrated by using a digital filter integrator to yield an estimate of the relative velocity. This two-step process is repeated once more to yield an estimate of the relative displacement measurement. To ensure equal signal conditioning of the time histories used in the estimation matrix, the relative

acceleration and base acceleration are also passed through the same high pass filter twice and the estimated relative velocity once more.

The high pass filters and integration introduce unwanted transients at the start and ends of the signal. These parts of the signal are removed. Typically, the first and last 10% of the signals are cropped. Further cropping of the signal may be used to use only specific regions of the time history that may be of interest (e.g., near resonance) in the estimation. The newly conditioned relative acceleration, velocity, displacement, forcing, and other terms are now ready to be used in the continuous-time system identification approach. When higher order models are being considered, derivatives of the acceleration signals are needed. In this case, a combination of low-pass filters to reduce high frequency noise and digital filter differentiators are used, and all of the signals receive the same amount of low-pass filtering, as with the high-pass filtering described above.

A4.2.3. Summary of the Continuous-Time Process

The general approach of applying the continuous-time system identification to estimate the system parameters is as follows:

1. Based on the physical system, derive an equation of motion with the appropriate stiffness, damping, and viscoelastic terms to model the desired dynamic behavior. The equation should be a function of measurable or derivable states (velocity, displacement, acceleration, or higher derivatives) and the model parameters. Ideally, it will be linear in parameters.
2. Derive the needed state space signals defined in the equation of motion. Be sure to condition the signals appropriately and filter all signals by an equal amount. Filters should be designed to reduce noise corruption and signals should be truncated to remove transient filter responses.
3. For the linear in parameters case, re-arrange the equation of motion so that all terms that are known are on the left hand side and all terms that are functions of the parameters are on the right hand side. Construct the vector q and the matrix A using the conditioned signals.
4. Depending on the structure of A , the matrix may become ill-conditioned. This results in MATLAB using a pseudo-inverse method to solve the system of equations and setting small singular values to zero, but these small terms may have important physical significance. To try to overcome this, it is recommended that the individual columns of A are divided by their respective standard deviation. The division will normalize the matrix such that all of the columns are of similar order and usually the estimation accuracy improves. Note that if the matrix A is normalized, the calculated vector p needs to be re-normalized to yield the correct stiffness and damping estimates.
5. By using a linear regression program (for example, *regress* in MATLAB) or something similar, solve the normal Equations A7 to yield estimates of p . When the parameters in p are functions of the physical parameters, it will be necessary to define a process to take the elements of \hat{p} to derive estimates of the system parameters of interest, for example, (k_1, k_2, \dots, c) .

6. Use the parameter estimates to calculate the system response by using, for example, a Runge Kutta algorithm with an appropriate step size. Compare the estimated response with the original response as an indication of the accuracy of the model. The difficult part is then to determine what model structure adjustments are needed to improve the predictions.

A4.2.4. Inclusion of the Viscoelastic Terms in Continuous-Time Estimation

One approach when $v(t)$ is not zero is to reformulate the integro-differential equation into a system of coupled ordinary differential equations. The continuous-time system identification approach can then be applied to estimate the system parameters. To reformulate the viscoelastic term, take the Laplace transform of Equation A5

$$v(t) = \sum_{i=1}^M f(t) * \beta_i e^{-\alpha_i t} \quad (\text{A9})$$

and note that the Laplace transform of a convolution (in time) is a multiplication in the s domain. Thus, the Laplace transform of Equation A9 is of the form:

$$V(s) = \sum_{i=1}^M F(s) \frac{\beta_i}{s + \alpha_i} = F(s) \frac{\mu_{M-1} s^{M-1} + \dots + \mu_0}{s^M + \gamma_{M-1} s^{M-1} + \dots + \gamma_0} \quad (\text{A10})$$

Multiplying through by the denominator of Equation A10, rearranging and taking the inverse Laplace transform yields the ordinary differential equation:

$$\frac{d^M v}{dt^M} + \gamma_{M-1} \frac{d^{M-1} v}{dt^{M-1}} + \dots + \gamma_0 v = \mu_{M-1} \frac{d^{M-1} f(t)}{dt^{M-1}} + \dots + \mu_0 f(t) \quad (\text{A11})$$

where μ_i and γ_i are combinations of α_i and β_i .

Prior to being able to apply the continuous-time system identification method to estimate k_i , c , μ_i and γ_i (and then α_i and β_i), Equation A2 is rearranged to express $v(t)$ as a function of terms that are themselves a function of z and its derivatives. It is then differentiated M times and substituted back to build an $(M + 2)$ th differential equation. Solving Equation A2 for $v(t)$, and differentiating yields:

$$v(t) = -m\ddot{y} - m\ddot{z} - k(z) - c(\dot{z}), \quad (\text{A12})$$

and

$$\dot{v}(t) = -m\ddot{y} - m\ddot{z} - \frac{d}{dt}[k(z)] - \frac{d}{dt}[c(\dot{z})], \quad (\text{A13})$$

etc.

Substituting Equation A12, Equation A13, etc. into Equation A4 results in the $(M + 2)$ th differential equation in z . For example, for Model 4a (with $M = 1$ and $N = 1$), the following system of equations may be constructed:

$$\begin{bmatrix} -m(\ddot{z}(\Delta) + \ddot{y}(\Delta)) \\ -m(\ddot{z}(2\Delta) + \ddot{y}(2\Delta)) \\ -m(\ddot{z}(3\Delta) + \ddot{y}(3\Delta)) \\ \vdots \\ -m(\ddot{z}(N\Delta) + \ddot{y}(N\Delta)) \end{bmatrix} = \begin{bmatrix} \ddot{z}(\Delta) & \dot{z}(\Delta) & z(\Delta) & m(\ddot{y}(\Delta)) \\ \ddot{z}(2\Delta) & \dot{z}(2\Delta) & z(2\Delta) & m(\ddot{y}(2\Delta)) \\ \ddot{z}(3\Delta) & \dot{z}(3\Delta) & z(3\Delta) & m(\ddot{y}(3\Delta)) \\ \vdots & \vdots & \vdots & \vdots \\ \ddot{z}(N\Delta) & \dot{z}(N\Delta) & z(N\Delta) & m(\ddot{y}(N\Delta)) \end{bmatrix} \begin{bmatrix} c + m\alpha_1 \\ k + c\alpha_1 \\ k\alpha_1 + \beta_1 \\ \alpha_1 \end{bmatrix} \quad (A14)$$

This is a linear system of equations, similar to Equation A7 but with the added complexity of having to transform the estimated parameters to estimates of c , k , α_i and β_i . Note that, in general, up to $(M + 2)$ th derivatives of the state space signals z and y are needed to construct this matrix, and while for the $M = 1$ the structure remains simple, increasing M increases the number of terms significantly and there are also signal and matrix conditioning problems when estimating high order derivatives. To avoid these problems, an iterative estimation approach was developed. This is described in Section A4.3.

A4.3. Estimation of Higher Order Viscoelastic Models

The previously described continuous-time system identification approach is not desirable for higher order models because the $(M + 2)$ th derivatives of the signals are needed and deriving these from measured acceleration signals can result in noise corruption of the signals [A5, A6]. To improve the estimation an iterative approach was developed. The parameter estimation is split into two parts. In one part, the stiffness and damping coefficients are estimated by using the continuous-system identification approach described in the previous section, and in the other part the impulse and/or frequency response of the viscoelastic kernel is modeled by using Prony Series estimation techniques. The estimated viscoelastic term $v(t)$ forms the bridge between the two parts of the estimation. A visual illustration of the iterative process is shown in Figure A3.

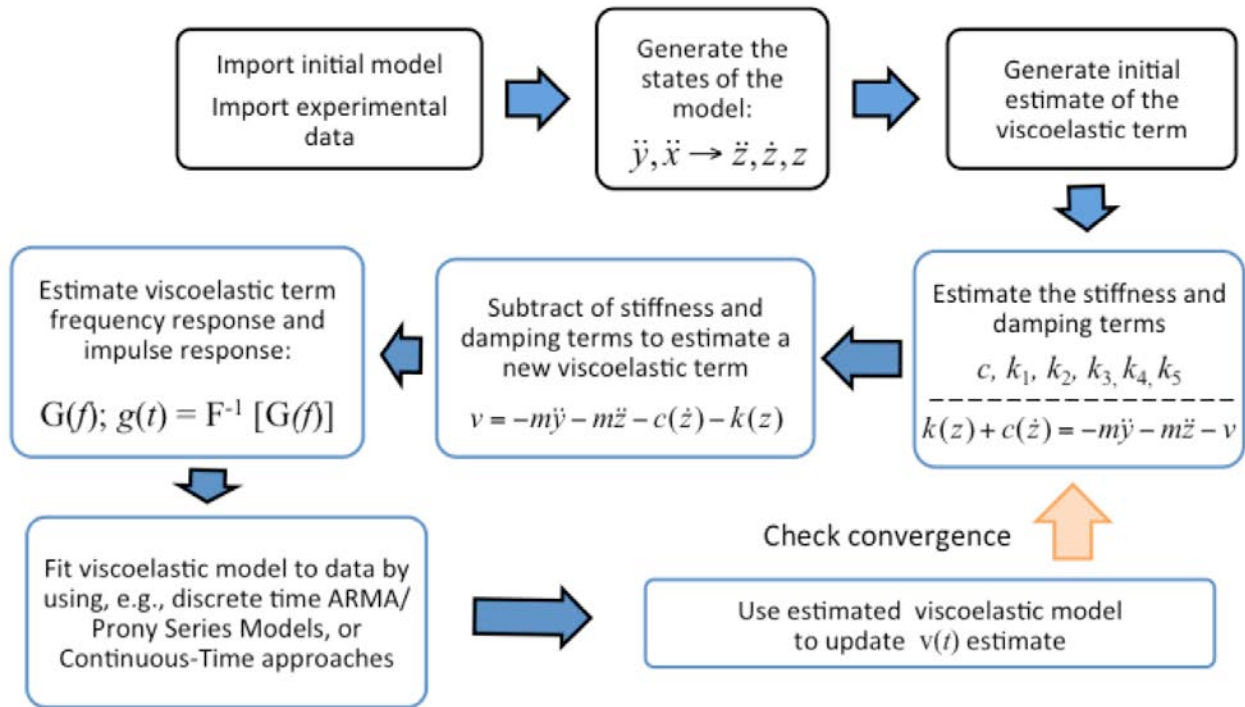


Figure A3. The steps in the iterative system identification approach used for parameter estimation. The black outlined boxes illustrate the initialization of the estimation, and the blue outlined boxes are the core of the iterative estimation scheme.

There are 10 steps in this estimation process, which are given below. Note that it is assumed that the base excitation frequency range and amplitude are sufficient to provide enough information to determine the system parameters. Note that it is straightforward to incorporate signals from different tests into the estimation process, which is helpful when trying to develop a single model of the system that predicts responses to different levels and types of excitation. In reality, the desired excitations will evolve as more is understood about the system behavior, model deficiencies are identified, and the proposed improved models and their identification are explored through simulation and analysis. Here, just the parameter estimation process is described for a given nonlinear and viscoelastic model structure.

Step 1: Import measured signals from experiments: relative acceleration $\ddot{z} = \ddot{x} - \ddot{y}$ and base acceleration \ddot{y} . Make sure to subtract any offset to ensure that the accelerations are centered about zero.

Step 2: Integrate the relative acceleration signals to calculate the states of the model, $\ddot{z}, \ddot{y} \rightarrow \dot{z}, z$ also, depending on model structure, calculate the necessary polynomial expressions of the signals (z^2, \dots , etc.).

Step 3: Assign an initial value to the viscoelastic term $v(t)$. Currently we are assuming the initial value of $v(t)$ is zero.

Step 4: By using the continuous-time system identification approach, estimate the stiffness and damping terms ($c; k_i; i = 1, 2, \dots, N$). Note that if high order polynomial expressions of the stiffness terms are considered, it will be particularly important to pay attention to the conditioning of the system matrix of Equations A7, prior to solving using the normal equations. This is accomplished by dividing each column by its respective standard deviation. Note, to compensate for this normalization, the estimates in the parameter vector \mathbf{p} will need to be multiplied by the corresponding standard deviations to yield estimates of the model parameters.

Step 5: Update the viscoelastic time history estimate by subtracting the damping and stiffness terms from the inertial terms: $\hat{v}(t) = -m\ddot{y} - m\ddot{z} - c(\dot{z}, z) - k(z)$.

Step 6: Calculate the viscoelastic kernel frequency response function, $G(f_k)$. If the signals are deterministic $G(f_k) = DFT[v(n\Delta)]/DFT[f(n\Delta)]$, or if the signals are random $G(f_k) = \hat{S}_{fv}/\hat{S}_{ff}$. Note that $DFT[-]$ denotes a Discrete Fourier Transform and \hat{S}_{ab} denotes the estimated cross spectral density between signal a and signal b . Segment averaging is used with Hann windows at a 50% overlap to estimate the cross and power spectral densities. An option in Step 7 is to directly fit to the impulse response of the viscoelastic kernel. An estimate of the impulse response is produced by applying an Inverse Discrete Fourier Transform $IDFT[-]$ to the estimated frequency response function and rearranging to place any acausal behavior (an outcome of all the filtering and signal conditioning) at the start of the impulse response.

Step 7: Fit an M_1 th order Prony Series model ($M_1 \gg M$) either to the frequency response function or to the impulse response function. Calculate the energy contributions of each term over a specified time period t_1 to t_2 of the impulse response. This time is specified to avoid any acausal behavior at the start and to not include too much of the region where the impulse response has decayed into the noise floor. In the estimation process it is possible for the viscoelastic terms to be either real or complex. Because the signal is real, complex terms appear in conjugate pairs. When terms are complex, the energy contribution of the complex conjugate pair is calculated. By energy, we mean the sum of the squared signal from t_1 to t_2 .

Step 8: Reduce the model order to M by sorting the viscoelastic terms by their energy contribution and selecting the terms with the highest individual energy contributions. Additional discussion on model reduction techniques and the challenges presented are included in subsection A4.3.1. [Note that there are some problems where two terms (or four complex terms) nearly cancel, thus their net contribution is small, but the individual contributions are large. Also, complex terms are sometimes associated with frequencies well outside the excitation region. Refinement of model term selection is a part of on-going research.]

Step 9: Check the convergence criteria. Currently this is specified to be a less than 0.1% change in the parameter estimates for the stiffness and damping terms, and a less than 1% change in the estimated viscoelastic parameters. These criteria are preset in the program. Increasing the tolerances decreases the computational time. Note that if the convergence criteria are too tight, the model will never converge and the parameter estimates will continue to oscillate between two values until maximum iteration number has been met.

Step 10: If convergence is not achieved, the viscoelastic term estimate is updated and the process returns to Step 4 and repeats.

A4.3.1. Prony Analysis and Model Order Reduction Discussion

There are many methods described in literature that can be used to reduce the model order of an estimated model, specifically with application to estimated Prony Series models. One main advantage of using Prony analysis is that it is a parametric method that fits a sum of exponentials, which is of the same structure as the viscoelastic hereditary kernel. When applied to a measurement, the Prony Series models both the signal structure and the noise structure, as well as any other artifacts introduced during the signal processing, and, in this case, impulse response estimation. Model reduction is desired because while a higher order model may result in an excellent fit to the measurements or estimated signals, many terms may have nothing to do with the behavior of the material. A simpler model that models the viscoelastic behavior of the material, as opposed to other artifacts, is desirable [A7, A8]. Extracting only these physical terms can be challenging.

Currently, we employ only individual term energy contributions as the criterion for developing an M th order viscoelastic kernel from a higher order M_1 th order model. The energy contribution terms are calculated for each term by squaring the signal and integrating over the same time interval for the system. When Prony Series terms appear in complex conjugate pairs the energy contribution of the pair is determined by:

$$E.C. = \int_{t_1}^{t_2} (A e^{-\alpha t} \cos(2\pi f t - \phi))^2 dt \quad (A15)$$

and for a real term the energy contribution is of the form,

$$E.C. = \int_{t_1}^{t_2} (A e^{-\alpha t})^2 dt \quad (A16)$$

When simulating the viscoelastic term, it is straightforward to choose the time interval for the energy contribution integral; however, when the viscoelastic term profile is unknown it is not as trivial. Ideally, the interval is chosen such that the initial transient behavior is ignored and the terms have decayed enough over the region of integration so that the amplitudes are in the noise floor. A very long interval is not wanted because eventually the integral will calculate energy contributions of the noise corruption. The nontrivial part is that the time interval must remain equal for all the contributing terms and be a good region for all terms.

As an example, the Prony Series analysis is applied to the experimentally determined viscoelastic impulse response resulting from testing on a pure-HTPB 76.2 mm (3 in) material sample with a 0.98 kg mass loading (corresponding to $m = 1.12$ kg). This system was excited at 5 g. After calculating the energy contribution of each term of the $M_1 = 250$ Prony Series estimation, the top ten contributing terms were selected and used to recreate the experimental impulse response. This is shown in Figure A4. Even with 10 terms, with the reduced order model it is possible to

predict the first few oscillations of the impulse response before it decays to the noise floor in the predicted impulse response.

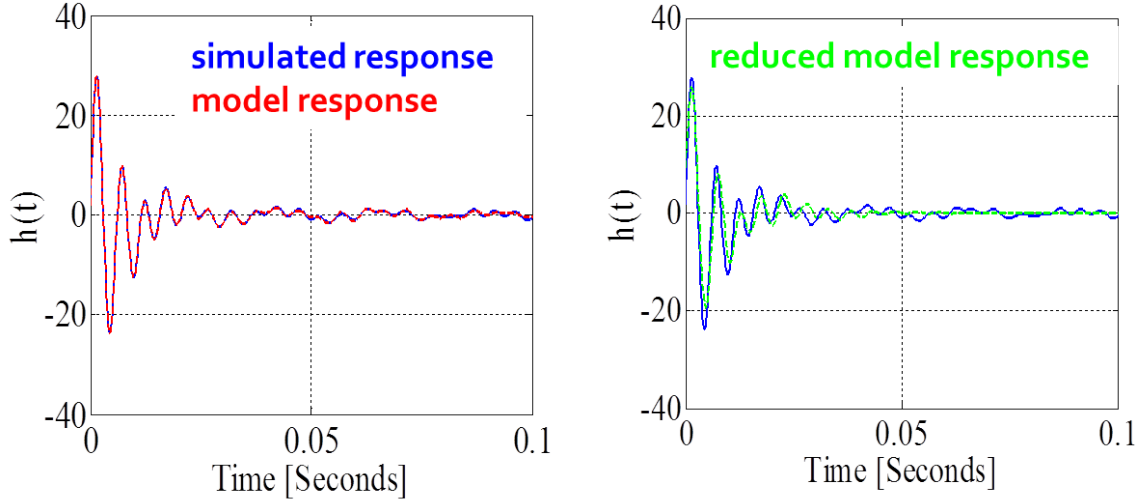


Figure A4. The impulse response of a pure-HTPB sample (blue) excited at 5 g along with the predicted Prony approximation for (left) $M_1 = 250$ (red) and (right) the top energy contributing terms, $M = 10$ (green)

Another approach is to fit directly to the estimated frequency response function. There are parts of the frequency response function that are heavily corrupted by noise and parts where the estimation is reasonably good (in the region of excitation). By doing the estimation in the frequency domain, we can select regions of the frequency response where the information is not strongly corrupted by noise.

The model of the sampled system transfer function that relates the sampled forcing function to the sampled viscoelastic function is determined by sampling the viscoelastic impulse response $g(t)$ and taking the z-transform of $g(n\Delta)$. It is of the form:

$$G(z) = \frac{b_0 + b_1 z^{-1} + \cdots + b_{M-1} z^{-(M-1)}}{1 + a_1 z^{-1} + \cdots + a_M z^{-M}} \quad (\text{A17})$$

Substituting

$$z = e^{j2\pi f/f_s}$$

where f is the frequency and f_s is the sampling frequency, gives the frequency response of the model:

$$G(z) = \frac{b_0 + b_1 e^{-j2\pi f/f_s} + \cdots + b_{M-1} e^{-j2\pi f(M-1)/f_s}}{1 + a_1 e^{-j2\pi f/f_s} + \cdots + a_M e^{-j2\pi fM/f_s}} \quad (A18)$$

Equation A18 can be rearranged and evaluated at frequencies $f = f_1, f_2, \dots, f_N$ and written in the form:

$$\begin{bmatrix} \hat{G}(f_1) \\ \hat{G}(f_2) \\ \vdots \\ \hat{G}(f_N) \end{bmatrix} = \begin{bmatrix} -\hat{G}(f_1)e^{-j2\pi f_1/f_s} & \dots & 1 & e^{-j2\pi f_1/f_s} & \dots & e^{-j2\pi(M-1)f_1/f_s} \\ -\hat{G}(f_2)e^{-j2\pi f_2/f_s} & \dots & 1 & e^{-j2\pi f_2/f_s} & \dots & e^{-j2\pi(M-1)f_2/f_s} \\ \vdots & \vdots & \vdots & \vdots & \vdots & \vdots \\ -\hat{G}(f_N)e^{-j2\pi f_N/f_s} & \dots & 1 & e^{-j2\pi f_N/f_s} & \dots & e^{-j2\pi(M-1)f_N/f_s} \end{bmatrix} \begin{bmatrix} a_1 \\ \vdots \\ a_M \\ b_0 \\ b_1 \\ \vdots \\ b_{M-1} \end{bmatrix}$$

where M is the model order, f_s is the sampling frequency and $\hat{G}(f_i)$ is the viscoelastic frequency response evaluated at f_i Hz. This can be written more simply as:

$$\{\mathbf{G}\} = [\mathbf{X}]\{\mathbf{P}\} \quad (A19)$$

Note that estimation errors due to noise and un-modelled dynamics when solving Equation A19 can sometimes yield complex imaginary coefficients. To prevent this, the matrix equation is reformulated to force the imaginary part of the coefficients equal to zero. The new matrix equation is of the form:

$$\begin{bmatrix} \text{Re}\{\hat{G}(f_1)\} \\ \text{Im}\{\hat{G}(f_1)\} \\ \vdots \\ \text{Re}\{\hat{G}(f_N)\} \\ \text{Im}\{\hat{G}(f_N)\} \end{bmatrix} = \begin{bmatrix} \text{Re}\{X_{11}\} & \text{Re}\{X_{12}\} & \dots & \dots & \dots \\ \text{Im}\{X_{11}\} & \text{Im}\{X_{12}\} & \dots & \dots & \dots \\ \vdots & \vdots & \vdots & \vdots & \vdots \\ \text{Re}\{X_{N1}\} & \text{Re}\{X_{N2}\} & \dots & \dots & \dots \\ \text{Im}\{X_{N1}\} & \text{Im}\{X_{N2}\} & \dots & \dots & \dots \end{bmatrix} \begin{bmatrix} a_1 \\ a_2 \\ \vdots \\ b_{M-2} \\ b_{M-1} \end{bmatrix} \quad (A20)$$

The model order reduction technique applied in the frequency domain is less sensitive to noise corruption than the Prony Series applied in the time domain. One explanation is that the selected frequency region is in the region of excitation and in this region the estimation is less corrupted by noise. When applying Prony Series analysis to experimental data in the frequency domain it was found that lower order viscoelastic models were sufficient to model the system behavior. The results of fitting a Prony Series model to the estimated viscoelastic frequency response function ($vFRF$) derived from testing on a pure-HTPB sample excited at 10 g with order $M_1 = 40$, and selecting only the top 10 contributing terms for varying regions of estimation is shown in Figure A5.

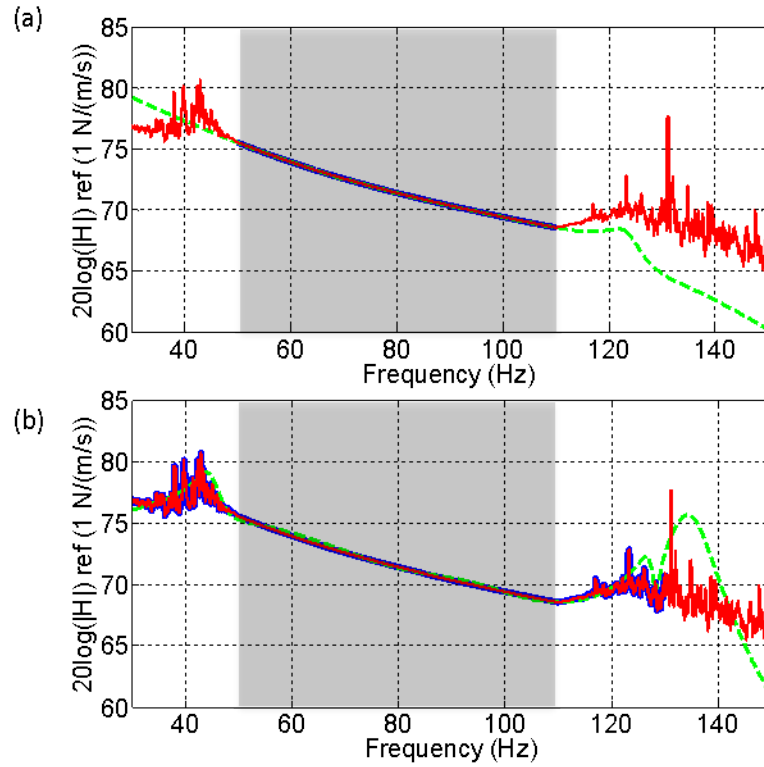


Figure A5. The viscoelastic kernel frequency response magnitudes ($|\nu FRF|$) derived from experiments on pure-HTPB excited at 10 g. The gray region denotes the region of strong excitation in the experiment, red is $|\nu FRF|$ derived as part of the iterative whole model estimation process, blue is the region used in the νFRF estimation process, and green is the $|\nu FRF|$ predicted using the estimated viscoelastic kernel model when fitting $M_1 = 40$ and selecting only the top 10 terms. The regions used in estimation: (a) 50-110 Hz, and (b) 30-130 Hz.

This viscoelastic kernel estimation and model order reduction has been incorporated into the model estimation process, but currently the user still has to specify a desired model order. Future work will include investigation of automatic selection of model order.

A5. 3D Numerical Implementation of Endochronic Constitutive Equations

A5.1. Endochronic Constitutive Equations and their Numerical Integration

The numerical integration of the endochronic constitutive equations follows the method reported by Hsu et al. [A9], modified to include rate-dependent (viscoplastic) effects.

In order to proceed with the numerical procedure, it is imperative to assume a functional form of the kernel function $\rho(z)$. According to Hsu et al. [A9], for numerical applications the kernel can be assumed to be expressed as the sum of a group of n exponentially decaying functions of the form:

$$\rho(z) = \sum_{r=1}^n C_r e^{-\alpha_r z} \quad (\text{A21})$$

Substituting the above approximation for $\rho(z)$ in Equation 1, we get

$$s = \sum_{r=1}^n \left[2 \int_0^z C_r e^{-\alpha_r(z-z')} \frac{d\epsilon^p}{dz'} dz' \right] \quad (\text{A22})$$

Let the loading be divided into m steps, and the following notations be used:

${}^k(\cdot)$: value of a variable at the end of k^{th} loading step ($k = 0, 1, 2 \dots m$).

${}^k(\Delta)$: increment in the value of variable caused by k^{th} loading step, i.e., ${}^k(\cdot) = {}^k(\cdot) - {}^{k-1}(\cdot)$.

Now, the integral in Equation A22 can be expressed approximately as:

$$\begin{aligned} \left[2 \int_0^z C_r e^{-\alpha_r(z-z')} \frac{d\epsilon^p}{dz'} dz' \right] &= 2 \sum_{k=1}^m \frac{{}^k(\Delta\epsilon^p)}{{}^k(\Delta z)} \int_{{}^{k-1}z}^{{}^kz} C_r e^{-\alpha_r({}^mz-z')} dz' \\ &= 2 \sum_{k=1}^m \frac{{}^k(\Delta\epsilon^p)}{{}^k(\Delta z)} \left[\frac{C_r}{\alpha_r} e^{-\alpha_r({}^mz-z')} \right]_{{}^{k-1}z}^{{}^kz} \\ &= 2 \sum_{k=1}^m \frac{C_r}{\alpha_r} \frac{{}^k(\Delta\epsilon^p)}{{}^k(\Delta z)} \left[e^{-\alpha_r({}^mz-{}^kz)} - e^{-\alpha_r({}^mz-{}^{k-1}z)} \right] \\ &= s^{(r)}({}^mz) \end{aligned} \quad (\text{A23})$$

Equations A22 and A23 can now be combined to give

$${}^m s \cong \sum_{r=1}^n {}^m s^{(r)} \quad (\text{A24})$$

the expression for ${}^m\mathbf{s}^{(r)}$ given by Equation A23 can be further simplified as

$$\begin{aligned}
{}^m\mathbf{s}^{(r)} &= 2 \sum_{k=1}^m \frac{C_r}{\alpha_r} \frac{{}^k(\Delta\epsilon^p)}{{}^k(\Delta z)} \left[e^{-\alpha_r({}^m z - {}^k z)} - e^{-\alpha_r({}^m z - {}^{k-1} z)} \right] \\
&= 2 \sum_{k=1}^m \frac{C_r}{\alpha_r} \frac{{}^k(\Delta\epsilon^p)}{{}^k(\Delta z)} \left[e^{-\alpha_r({}^{m-1} z - {}^k z)} - e^{-\alpha_r({}^{m-1} z - {}^{k-1} z)} \right] e^{-\alpha_r {}^m(\Delta z)} \\
&\quad + 2 \frac{C_r}{\alpha_r} \frac{{}^k(\Delta\epsilon^p)}{{}^k(\Delta z)} \\
&= {}^{m-1}\mathbf{s}^{(r)} e^{-\alpha_r {}^m(\Delta z)} + 2 \frac{C_r}{\alpha_r} \frac{{}^k(\Delta\epsilon^p)}{{}^k(\Delta z)} (1 - e^{-\alpha_r {}^m(\Delta z)})
\end{aligned} \tag{A25}$$

In Equation A25, for the case of $\alpha_r = 0$, L'Hospital's rule can be applied to calculate ${}^m\mathbf{s}^{(1)}$. Looking at Equations A24 and A25, it can be concluded that once ${}^m(\Delta z)$ and ${}^m(\Delta\epsilon^p)$ are known, ${}^m\mathbf{s}^{(r)}$ can be calculated by using ${}^{m-1}\mathbf{s}^{(r)}$, the value at the end of the previous loading step. Thus only the value of $\mathbf{s}^{(r)}$ at the end of the previous step needs to be stored, which greatly simplifies the numerical procedure.

From the point of view of computer simulation, the computer code for the model should be able to take the increment in value of any six components of the stress and strain tensors as input and provide as output the incremental values of the remaining six components, plastic strain tensor components, intrinsic time scale and measure, and deviatoric stress components. In order to write such a code, incremental equations are needed. First, the incremental equation for the deviatoric stress can be given by

$$\begin{aligned}
{}^m(\Delta\mathbf{s}) &= {}^m\mathbf{s} - {}^{m-1}\mathbf{s} = \sum_{r=1}^n {}^m\mathbf{s}^{(r)} - \sum_{r=1}^n {}^{m-1}\mathbf{s}^{(r)} \\
&= \sum_{r=1}^n {}^{m-1}\mathbf{s}^{(r)} e^{-\alpha_r {}^m(\Delta z)} + 2 \left[\frac{1}{{}^m(\Delta z)} \sum_{r=1}^n \frac{C_r}{\alpha_r} (1 - e^{-\alpha_r {}^m(\Delta z)}) \right] {}^m(\Delta\epsilon^p) \\
&\quad - \sum_{r=1}^n {}^{m-1}\mathbf{s}^{(r)} \\
\Rightarrow {}^m(\Delta\mathbf{s}) &= 2 \left[\frac{1}{{}^m(\Delta z)} \sum_{r=1}^n \frac{C_r}{\alpha_r} (1 - e^{-\alpha_r {}^m(\Delta z)}) \right] {}^m(\Delta\epsilon^p) \\
&\quad + \sum_{r=1}^n {}^{m-1}\mathbf{s}^{(r)} (e^{-\alpha_r {}^m(\Delta z)} - 1)
\end{aligned} \tag{A26}$$

where

$${}^m(\Delta\mathbf{s}) = {}^m(\Delta\sigma) - \frac{1}{3} \mathbf{tr}({}^m(\Delta\sigma)) \mathbf{I} \tag{A27}$$

The incremental equations for total stress and total strain are given by:

$$m(\Delta\epsilon) = m(\Delta\epsilon^e) + m(\Delta\epsilon^p) \quad (\text{A28})$$

and

$$m(\Delta\sigma) = \lambda \operatorname{tr}(m(\Delta\epsilon^e)) + 2\mu(m(\Delta\epsilon^e)) \quad (\text{A29})$$

The increments in intrinsic time scale $m(\Delta z)$ and intrinsic time measure $m(\Delta\zeta)$ are related as:

$$m(\Delta z) = \frac{m(\Delta\zeta)}{f\left(m^{-1}\zeta + \beta m(\Delta\zeta), \frac{\Delta\zeta}{\Delta t}\right)} \quad (\text{A30})$$

where $0 \leq \beta \leq 0.5$ for hardening materials (will be explained later), and

$$m(\Delta\zeta) = \sqrt{m(\Delta\epsilon^p) : m(\Delta\epsilon^p)} \quad (\text{A31})$$

Next, a numerical procedure will be formulated using the above incremental equations. Using Equations A28 and A29, we have

$$m\{\Delta\sigma\} = \mathbf{C}[m\{\Delta\epsilon\} - m\{\Delta\epsilon^p\}] \quad (\text{A32})$$

where $m\{\Delta\sigma\}$ is a vector of six independent stress components

$$m\{\Delta\sigma\} = [\Delta\sigma_{11} \Delta\sigma_{22} \Delta\sigma_{33} \Delta\sigma_{23} \Delta\sigma_{13} \Delta\sigma_{12}]^T \quad (\text{A33})$$

Vectors $m\{\Delta\epsilon\}$ and $m\{\Delta\epsilon^p\}$ are defined in the same manner for total strain and plastic strain respectively. \mathbf{C} is a matrix of elastic constants given by

$$\mathbf{C} = \begin{bmatrix} \lambda + 2\mu & \lambda & \lambda & 0 & 0 & 0 \\ \lambda & \lambda + 2\mu & \lambda & 0 & 0 & 0 \\ \lambda & \lambda & \lambda + 2\mu & 0 & 0 & 0 \\ 0 & 0 & 0 & \mu & 0 & 0 \\ 0 & 0 & 0 & 0 & \mu & 0 \\ 0 & 0 & 0 & 0 & 0 & \mu \end{bmatrix} \quad (\text{A34})$$

Then, using Equations A27, A28, and A29, and the condition of plastic incompressibility, we get

$$m(\Delta\epsilon) = \frac{1}{2\mu} m(\Delta s) + m(\Delta\epsilon^p) \quad (\text{A35})$$

where ${}^m(\Delta e)$ is the matrix of deviatoric strain increments given by

$${}^m(\Delta e) = {}^m(\Delta \epsilon) - \frac{1}{3} \operatorname{tr}({}^m(\Delta \epsilon)) \mathbf{I} \quad (\text{A36})$$

Substituting the expression for $m(\Delta s)$ from Equation A35 into the incremental equation for $m(\Delta s)$, Equation A26, we have

$$\begin{aligned} 2\mu[{}^m(\Delta \epsilon) - {}^m(\Delta \epsilon^p)] \\ = 2 \left[\frac{1}{m(\Delta z)} \sum_{r=1}^n \frac{C_r}{\alpha_r} (1 - e^{-\alpha_r m(\Delta z)}) \right] {}^m(\Delta \epsilon^p) \\ + \sum_{r=1}^n {}^m s^{(r)} (e^{-\alpha_r m(\Delta z)} - 1) \end{aligned} \quad (\text{A37})$$

Rearranging the above equation, we have

$$\mu({}^m(\Delta e)) + \frac{1}{2} \sum_{r=1}^n {}^m s^{(r)} (e^{-\alpha_r m(\Delta z)} - 1) = \left[\mu + \sum_{r=1}^n \frac{C_r}{\alpha_r} \frac{(1 - e^{-\alpha_r m(\Delta z)})}{m(\Delta z)} \right] {}^m(\Delta \epsilon^p) \quad (\text{A38})$$

Taking the inner product of Equation A38 with itself, we get

$$\langle \mathbf{A}, \mathbf{A} \rangle = B^2 \frac{{}^m(\Delta \zeta)^2}{m(\Delta z)^2} \quad (\text{A39})$$

where

$$\mathbf{A} = \mu({}^m(\Delta e)) + \frac{1}{2} \sum_{r=1}^n {}^m s^{(r)} (e^{-\alpha_r m(\Delta z)} - 1) \quad (\text{A40})$$

and

$$B = \mu({}^m z) + \sum_{r=1}^n \frac{C_r}{\alpha_r} (1 - e^{-\alpha_r m(\Delta z)}) \quad (\text{A41})$$

The incremental relation between z and ζ can be expressed as

$$\Delta z = \frac{\Delta \zeta}{f\left({}^m \zeta + \beta \Delta \zeta, \frac{\Delta \zeta}{\Delta t}\right)} \quad (\text{A42})$$

where $\beta \geq 1/2$. Using Equation A42 in Equation A39, we get

$$R(\Delta z) = \langle \mathbf{A}, \mathbf{A} \rangle - B^2 f^2 \left({}^m \zeta + \beta \Delta \zeta, \frac{\Delta \zeta}{\Delta t} \right) = 0 \quad (\text{A43})$$

Equation 43, being a nonlinear equation in single variable, can now be solved for Δz by a fail-safe method (a combination of bisection and Newton-Raphson's method). The expressions for the derivatives needed to solve the equation are

$$\frac{\partial R}{\partial \Delta z} = 2 \left[\left\langle \frac{\partial \mathbf{A}}{\partial \Delta z}, \mathbf{A} \right\rangle - 2fB \left(\frac{\partial B}{\partial \Delta z} f + B \frac{\partial f}{\partial \Delta z} \right) \right] \quad (\text{A44})$$

$$\frac{\partial \mathbf{A}}{\partial \Delta z} = \frac{1}{2} \sum_{r=1}^n \alpha_r {}^m \mathbf{s}^{(r)} e^{-\alpha_r \Delta z} \quad (\text{A45})$$

$$\frac{\partial B}{\partial \Delta \zeta} = \mu + \sum_{r=1}^n C_r e^{-\alpha_r z} \quad (\text{A46})$$

$$\frac{\partial f \left({}^m \zeta + \beta \Delta \zeta, \frac{\Delta \zeta}{\Delta t} \right)}{\partial \Delta z} = \frac{f \left(\beta \frac{\partial f}{\partial \zeta} + \frac{1}{\Delta t} \frac{\partial f}{\partial \dot{\zeta}} \right)}{1 - \Delta z \left(\beta \frac{\partial f}{\partial \zeta} + \frac{1}{\Delta t} \frac{\partial f}{\partial \dot{\zeta}} \right)} \quad (\text{A47})$$

Once Δz is obtained, it can be used to calculate the desired plastic strain increment

$$\epsilon_{ij}^p = \frac{A_{ij} \Delta z}{B} \quad (\text{A48})$$

The algorithm is depicted in Figure A6. The main aspect of this numerical scheme is that a positive root is guaranteed at every loading step regardless of the step size.

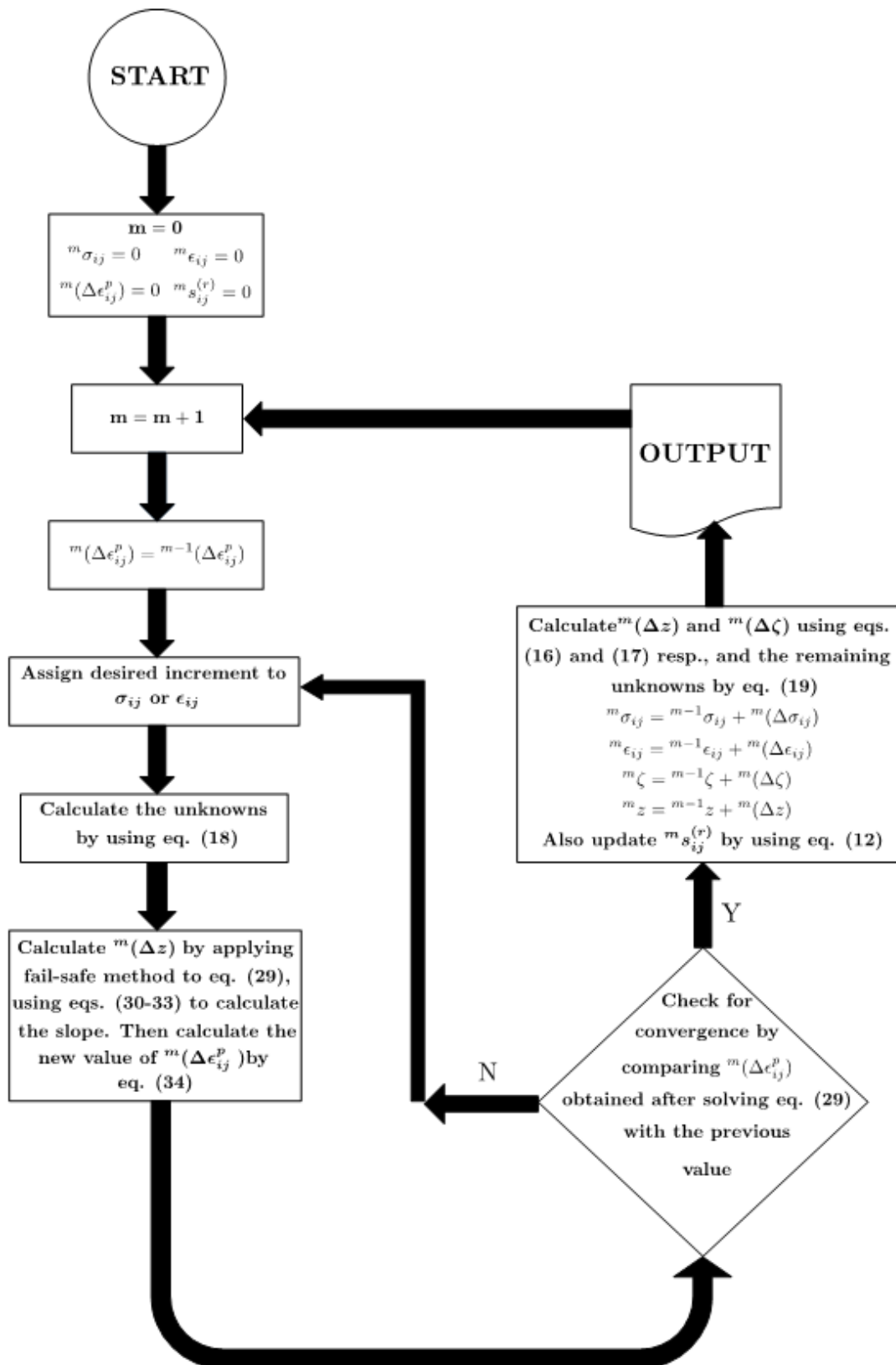


Figure A6. Flowchart of the algorithm used for the endochronic numerical implementation

A5.2. Calibration of the Material Kernel and Hardening Functions

A.5.2.1. Calibration of the Kernel Function

As discussed previously, the endochronic kernel function $\rho(z)$ is defined in the form of a sum of a finite number of exponentially decaying functions of the form:

$$\rho(z) = \sum_{r=1}^n C_r e^{-\alpha_r z} \quad (\text{A49})$$

In order to calibrate this function, we need to find the value of parameters C_r and α_r in such a way that the difference between the model predictions and experimental measurements is minimized. For most practical purposes, the energetic composite materials should be subjected to axial loading, hence calibration with respect to uni-axial cyclic loading experimental data should be sufficient. According to Jao et al. [A10], an optimization problem can be formulated in the following manner

$$\min F(\boldsymbol{v}) = \sum_{i=1}^m w_i [\sigma(\boldsymbol{v}, \boldsymbol{\epsilon}_{exp}) - \sigma_{exp}]^2 \quad (\text{A50})$$

subject to

$$f_j(\boldsymbol{v}) = 0; j = 1, 2, \dots, p \quad (\text{A51})$$

$$g_l(\boldsymbol{v}) \leq 0; l = 1, 2, \dots, q \quad (\text{A52})$$

where $F(\boldsymbol{v})$ is the objective function to be minimized, w_i represents the weight to be applied to i^{th} data point, $\boldsymbol{v} = \{C_r, \alpha_r\}^T$ is a vector of the unknown kernel parameters, $\sigma(\boldsymbol{v}, \boldsymbol{\epsilon})$ and σ_{exp} represent the model prediction and experimental measurement of stress respectively, and f_j and g_l respectively represent the equality and inequality constraints enforced on the kernel parameters. Unlike Jao [A10], it has been assumed here that the hardening function is already calibrated and known, and hence the only parameters that need to be determined are the kernel parameters.

The above minimization problem can be solved efficiently in MATLAB by using the inbuilt constrained minimization function *fmincon*. The complete procedure can be summarized in the following steps:

- Choose the number of kernel terms and take an initial guess \boldsymbol{v}_0 of kernel parameters.
- Specify the upper and lower bounds on the kernel parameters. These are the constraints $g_l(\boldsymbol{v})$ imposed on the objective function (There are no equality constraints in this particular problem, hence $j = 0$).
- For each loading step, calculate the uni-axial stress from the 3D endochronic numerical implementation, using uni-axial strain input from experimental data to obtain $\sigma(\boldsymbol{v}_0, \boldsymbol{\epsilon}_{exp})$.
- Obtain the kernel parameters that minimize the objective function $F(\boldsymbol{v})$ using *fmincon*.

A5.2.2. Calibration of the Hardening Function

After determination of kernel parameters C_r and α_r , the hardening function $f(\zeta, \dot{\zeta})$ is calibrated by using the transient cyclic hardening response. A large number of data points $(\sigma_{11}, \varepsilon_{11})$ are read from the experimental cyclic hardening curves at different strain rates. Then, stress and strain increments $(\Delta\sigma_{11}, \Delta\varepsilon_{11})$ are determined between two consecutive points for the entire data. $\Delta\varepsilon_{11}^p$ is then determined for each of the values by using Equation A32. Now, by substituting ${}^m(\Delta z)$ in Equation A39 using Equation A30, we have

$$\begin{aligned} {}^m(\Delta\sigma)_{11} & {}^m(\Delta\sigma)_{11} \\ &= 3 \left[\frac{f}{{}^m(\Delta\zeta)} \sum_{r=1}^n \frac{C_r}{\alpha_r} \left(1 - e^{-\alpha_r \frac{{}^m(\Delta\zeta)}{f}} \right) \right] {}^m(\Delta\varepsilon_{11}^p) \\ &+ \frac{3}{2} \sum_{r=1}^n {}^{m-1}s_{11}^{(r)} \left(e^{-\alpha_r \frac{{}^m(\Delta\zeta)}{f}} - 1 \right) \end{aligned} \quad (\text{A53})$$

where ${}^m(\Delta\zeta) = \sqrt{\frac{3}{2}} |{}^m(\Delta\varepsilon_{11}^p)|$. Since ${}^m(\Delta\varepsilon_{11}^p)$ and ${}^m(\Delta\sigma)_{11}$ are already known for all the data points and ${}^{m-1}s_{11}^{(r)}$ is determined in the previous step, Equation (44) reduces to a nonlinear equation in only one unknown, f . Thus the value of f can be determined at each step for complete experimental data at each strain rate by numerically solving Equation (44) by either the bisection method or Newton-Raphson's method. It can be assumed that for a particular step $(m-1) \rightarrow m$, the calculated value of f corresponds to a value of

$${}^m\zeta = {}^{m-1}\zeta + \beta({}^m(\Delta\zeta)) \quad (\text{A54})$$

where $\beta = 1/2$ is a reasonable approximation (Hsu et al. [A9]). Now, values of f corresponding to various data points on the stress-strain curves of each strain rate can be plotted against $(\zeta, \dot{\zeta})$, and the hardening function $f(\zeta, \dot{\zeta})$ is determined by 2D linear piecewise fitting to the plot.

A.5.2. Staggered Algorithm for Simultaneous Calibration of the Kernel and Hardening Functions

In the previous sections we have discussed the calibration procedure for the kernel and hardening function parameters, and have seen that the two functions are interdependent for the purpose of calibration. We assumed there that the calibrated hardening function was available for the kernel function and the calibrated kernel function was available for the hardening function. However, in practice we would need to calibrate both of the functions at the same time. This problem was efficiently tackled through a staggered algorithm that could simultaneously calibrate both the kernel and hardening functions. Figure A7 provides a description of the algorithm. The iterative procedure starts with an initial guess of the kernel parameters, which along with uni-axial cyclic loading experimental data, is provided as an input for calibration of the hardening function. The calibrated hardening function, along with the initial guess of kernel parameters and experimental data serve as an input to the optimization problem that yields a new set of kernel parameters. The

procedure is iterated until the error, denoted by the l^2 norm of the difference between the kernel parameters of the current and previous guess converges within a specified tolerance.

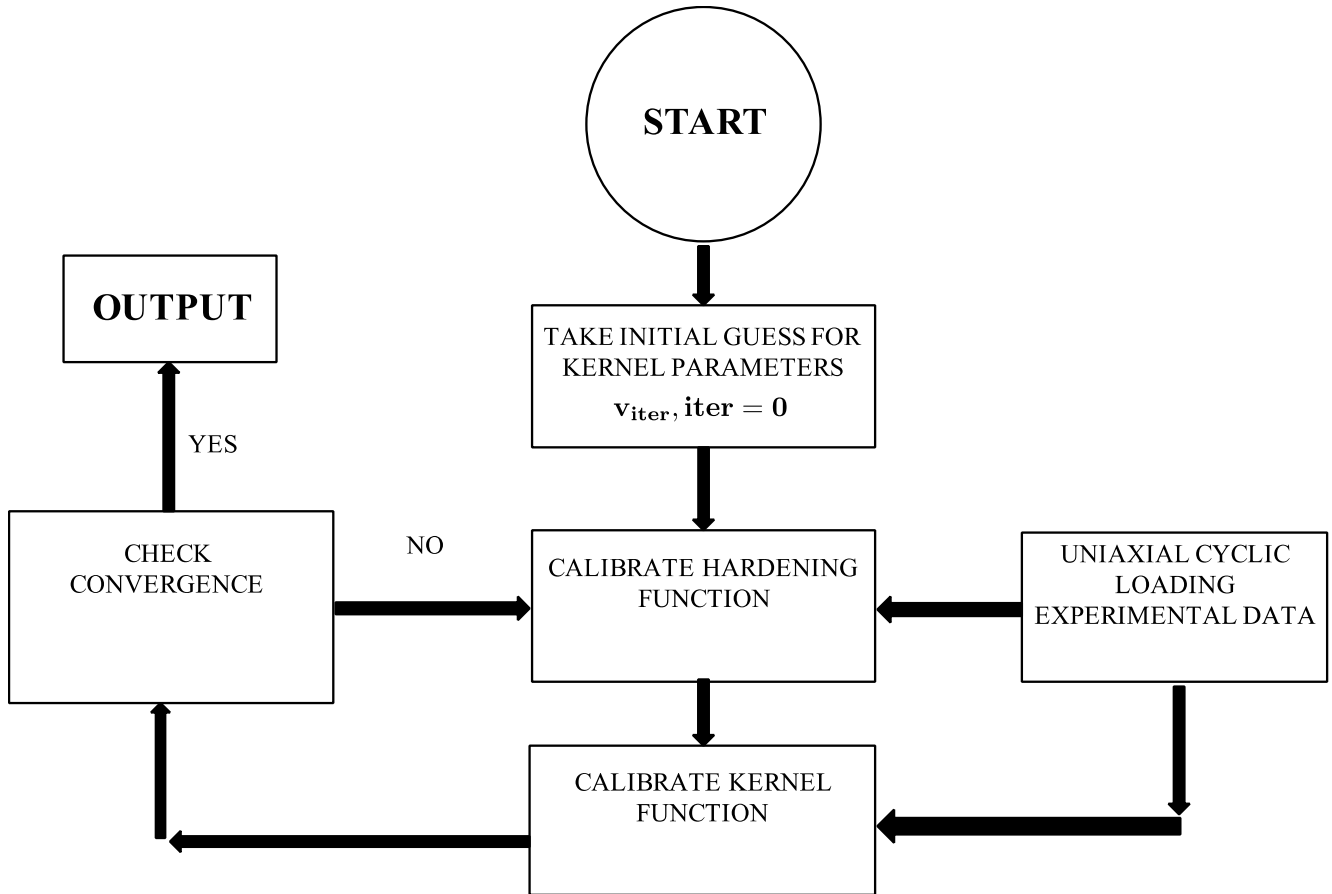


Figure A7. The staggered algorithm used for the simultaneous calibration of the endochronic kernel and hardening functions

A6. REFERENCES

- A1. J. Paripovic and P. Davies. Identification of the dynamic behavior of surrogate explosive materials. IDETC 2013: The ASME 2013 International Design Engineering Technical Conferences and Computers and Information in Engineering Conference. 2013. DETC2013-12755.
- A2. R. Widdle. Measurement and modeling of the mechanical properties of the polyurethane foam. Ph.D. Dissertation. 2005. Purdue University.
- A3. J. Paripovic. Identification of the dynamic behavior of surrogate explosive materials. M.S. Thesis. 2013. Purdue University.
- A4. T. Doughty. System identification of modes in non-linear structures. Ph.D. Dissertation. 2002. Purdue University.
- A5. Y. Azizi, A. K. Bajaj, P. Davies, and V. Sundaram. Prediction and verification of the periodic response of a single-degree-of-freedom foam-mass system by using incremental harmonic balance. *Nonlinear Dynamics*. 2015. **82**(4): p. 1933–1951.
- A6. Y. Azizi, P. Davies, and A. K. Bajaj. Identification of nonlinear viscoelastic models of flexible polyurethane foam from uniaxial compression data. IMECE 2012: The ASME 2012 International Mechanical Engineering Congress and Exposition. 2012. p. 447–454.
- A7. D. Trudnowski. Order reduction of large-scale linear oscillatory system models. *IEEE Transactions on Power Systems*. 1994. **9**(1): p. 451–458.
- A8. D. A. Pierre, D. J. Trudnowski, and J. F. Hauer. Identifying linear reduced-order models for systems with arbitrary initial conditions using Prony signal analysis. *IEEE Transactions on Automatic Control*. 1992. **37**(6): p. 831–835.
- A9. S. Y. Hsu, S. K. Jain, and O. H. Griffin. Verification of endochronic theory for non-proportional loading paths. ASCE Journal of Engineering Mechanics. 1991. **117**(1): p. 110–131.
- A10. S. Y. Jao, J. S. Arora, and H. C. Wu. An optimization approach for material-constant determination for the endochronic constitutive model. *Computational Mechanics*. 1991. **8**(1): p. 25-41.

DISTRIBUTION LIST
AFRL-RW-EG-TR-2016-088

*Defense Technical Info Center
8725 John J. Kingman Rd Ste 0944
Fort Belvoir VA 22060-6218

AFRL/RWME (1)
AFRL/RWORR (STINFO Office) (1)